Highlights

A disordered kinetic model for clumped isotope bond reordering in carbonates

Jordon D. Hemingway, Gregory A. Henkes

- Clumped isotope reordering kinetics arise from random-walk ^{18}O diffusion
- Carbonate clumped isotope bond reordering is modeled using disordered kinetics
- All previous models are shown to be specific cases of disordered kinetics
- Calcite & dolomite rate coefficient distributions are well-approximated as lognormal
- Disordered kinetics improves *t*-*T* predictions of natural samples

A disordered kinetic model for clumped isotope bond reordering in carbonates

Jordon D. Hemingway[a,b,1,*], Gregory A. Henkes[c,1,*]

[a]*Department of Earth and Planetary Sciences, Harvard University, Cambridge, Massachusetts, USA*
[b]*Geological Institute, Department of Earth Sciences, ETH Zurich, Zurich, Switzerland*
[c]*Department of Geosciences, Stony Brook University, Stony Brook, New York, USA*

Abstract

Carbonate clumped isotopes (Δ_{47}) have become a widely applied method for paleothermometry, with applications spanning many environmental settings over hundreds of millions of years. However, Δ_{47}-based paleothermometry can be complicated by closure temperature-like behavior whereby C–O bonds are reset at elevated diagenetic or metamorphic temperatures, sometimes without obvious mineral alteration. Laboratory studies have constrained this phenomenon by heating well-characterized materials at various temperatures, observing temporal Δ_{47} evolution, and fitting results to kinetic models with prescribed C–O bond reordering mechanisms. While informative, these models are inflexible regarding the nature of isotope exchange, leading to potential uncertainties when extrapolated to geologic timescales. Here, we instead propose that observed reordering rates arise naturally from random-walk ^{18}O diffusion through the carbonate lattice, and we develop a "disordered" kinetic framework that treats C–O bond reordering as a continuum of first-order processes occurring in parallel at different rates. We show theoretically that all previous models are specific cases of disordered kinetics; thus, our approach reconciles the transient defect/equilibrium defect and paired reaction-diffusion models. We estimate the rate coefficient distributions from published heating experiment data by finding a regularized inverse solution that best fits each Δ_{47} timeseries without assuming a particular functional form *a priori*. Resulting distributions are well-approximated as lognormal for all experiments on calcite or dolomite; aragonite experiments require more complex distributions that are consistent with a change in oxygen bonding environment during the transition to calcite. Presuming lognormal rate coefficient distributions and Arrhenius-like temperature dependence yields an underlying activation energy, E, distribution that is Gaussian with a mean value of $\mu_E = 224.3 \pm 27.6$ kJ mol^{-1} and a standard deviation of $\sigma_E = 17.4 \pm 0.7$ kJ mol^{-1} ($\pm 1\sigma$ uncertainty; $n = 24$) for calcite and $\mu_E = 230.3 \pm 47.7$ kJ mol^{-1} and $\sigma_E = 14.8 \pm 2.2$ kJ mol^{-1} ($n = 4$) for dolomite. These model results are adaptable to other minerals and may provide a basis for future experiments whereby the nature of carbonate C–O bonds is altered (e.g., by inducing mechanical strain or cation substitution). Finally, we apply our results to geologically relevant heating/cooling histories and suggest that previous models underestimate low-temperature alteration but overestimate Δ_{47} blocking temperatures.

Keywords: activation energy model, carbonate, apparent equilibrium temperature, clumped isotopes, solid-state

diffusion, thermometry

1. Introduction

Carbonate clumped isotope ratios (reported as Δ_{47}) are a valuable paleothermometer because they have been shown—empirically and experimentally—to solve the underdetermination problem with carbonate-water oxygen isotope exchange thermometry (Eiler, 2011). This apparent panacea, however, comes with caveats. Specifically, clumped isotopes are subject to alteration during diagenetic dissolution-reprecipitation of the original carbonate, both in water-buffered and rock-buffered settings (e.g., Ryb and Eiler, 2018; Shenton et al., 2015), and by internal, diffusion-driven isotope exchange reactions within the solid mineral lattice at elevated temperatures—so-called "solid-state clumped isotope bond reordering" (Dennis and Schrag, 2010; Passey and Henkes, 2012; Stolper and Eiler, 2015; Brenner et al., 2018; Lloyd et al., 2018; Chen et al., 2019).

Bond reordering has been observed or hypothesized to affect carbonates from many geologic contexts on Earth. Empirical evidence comes from two main sources: (i) carbonatites, where Δ_{47}-derived temperatures, $T(\Delta_{47})$, are consistently much lower than inferred igneous crystallization temperatures (Dennis and Schrag, 2010; Stolper and Eiler, 2015; Fosu et al., 2020), and (ii) marbles and sedimentary rock alteration along dikes, where $T(\Delta_{47})$ systematically increases closer to the heat source (Finnegan et al., 2011; Lloyd et al., 2017; Ryb et al., 2017). Furthermore, bond reordering has been invoked to explain elevated $T(\Delta_{47})$ in deeply buried paleoclimate archives (e.g., shells) that are petrographically and geochemically well-preserved (e.g., Shenton et al., 2015; Henkes et al., 2014, 2018). Predicting the impact of bond reordering on measured Δ_{47} values is thus critically important for properly interpreting clumped isotope paleotemperature records, particularly in older archives that may have been exposed to higher diagenetic temperatures (Henkes et al., 2018).

Quantifying bond reordering necessitates kinetic models that both satisfy experimental tests and are amenable to a wide range of geologic applications. This has been achieved in the laboratory by heating the same mineralogically pure carbonate material at multiple temperatures for discrete time intervals. From these studies, it is possible to observe Δ_{47} evolution without obvious physical or isotopic changes to the reactant (i.e., decarbonation or mineral-gas/mineral-liquid isotope exchange). By assuming first-order kinetics and Arrhenius-like temperature dependence, one can utilize heating experiment results to estimate E, the underlying activation energy of clumped isotope bond reordering, and k_0, the Arrhenius pre-exponential factor (Passey and Henkes, 2012; Stolper and Eiler, 2015). Given

*Corresponding authors
Email addresses: jhemingway@ethz.ch (Jordon D. Hemingway), gregory.henkes@stonybrook.edu (Gregory A. Henkes)
[1]These authors contributed equally to this work

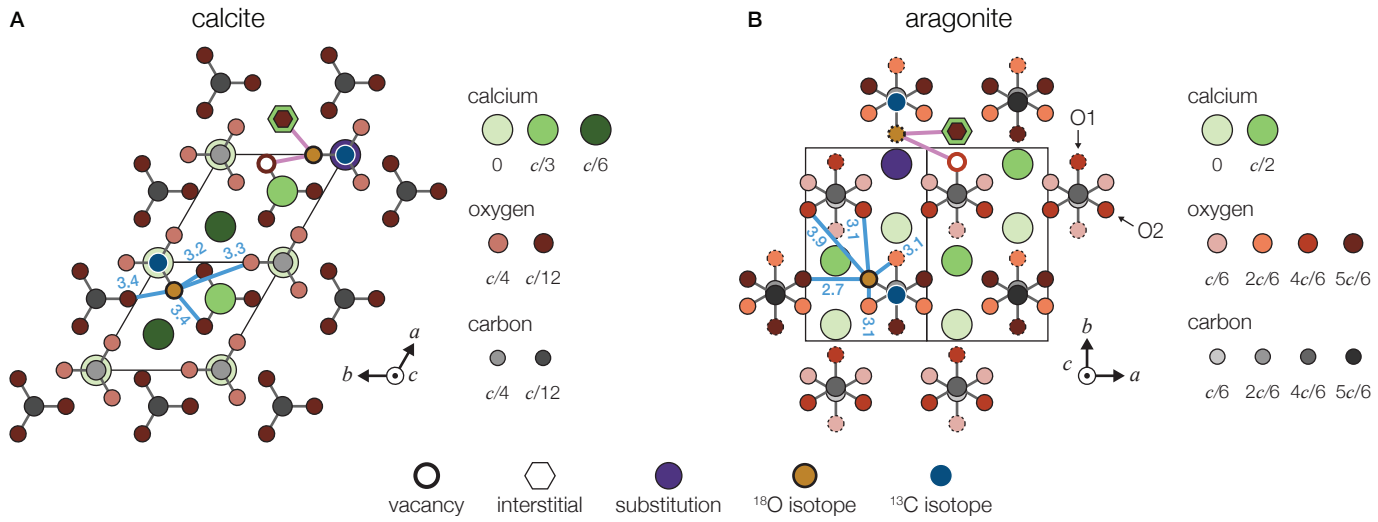

Figure 1: Crystal structures of (**A**) calcite and (**B**) aragonite, each showing two unit cells projected onto the (001) plane. Carbon (grays), oxygen (reds), and calcium (greens) atoms are shaded according to their distance along the c axis. Isotopically substituted oxygens (^{18}O) and carbons (^{13}C) are shown in gold and blue, respectively. Also included are representations of crystal lattice defects that may influence oxygen bonding environments and clumped isotope reordering rates: calcium substitutions (e.g., Mg^{2+} or Sr^{2+}; purple), oxygen vacancies (open circles), and interstitial atoms (hexagons). Interactions between an ^{18}O atom and neighboring defects are highlighted with pink lines, whereas bond distances (in Angstroms) between an ^{18}O atom and all nearest neighbor O atoms are highlighted with light blue lines (Markgraf and Reeder, 1985; De Villiers, 1971). For aragonite, O1 type oxygens are outlined in dotted lines, whereas O2 type oxygens are outlined in solid lines. Dolomite crystal structure is similar to that of calcite but with the $c/6$ calcium replaced by magnesium.

these experimentally determined Arrhenius parameters, Δ_{47} evolution due to bond reordering can then be estimated for any carbonate sample that has experienced any specified time-temperature (t-T) history (Passey and Henkes, 2012; Stolper and Eiler, 2015).

However, nearly all heating experiments to date are complicated by the presence of an early, rapid change in Δ_{47} that appears to deviate from exponential decay predicted by first-order kinetics (Passey and Henkes, 2012; Henkes et al., 2014; Stolper and Eiler, 2015; Lloyd et al., 2018). While initially ignored, these early data points have prompted the development of two alternative bond reordering models. First, the "transient defect/equilibrium defect" model of Henkes et al. (2014) posits that non-first order behavior results from the simultaneous reaction of two defect populations: one that follows first-order kinetics and a second whose concentration decreases with prolonged heating. Despite its presence, Passey and Henkes (2012) and Henkes et al. (2014) argue that the nature of this transient defect pool is ambiguous and likely annealed in many geologic contexts. Second, the "paired reaction-diffusion" model of Stolper and Eiler (2015) treats the early, rapid change in experimental Δ_{47} as the result of interactions between pairs of neighboring, singly substituted carbonate groups; these groups can then diffuse through the crystal lattice according to first-order kinetics. This model is intuitive and capable of capturing Δ_{47} changes in most experimental datasets but is inflexible and disregards the contribution of lattice defects or other extrinsic factors that may promote isotope exchange. Importantly, both models prescribe C–O bond reordering mechanisms *a priori*, potentially leading to large

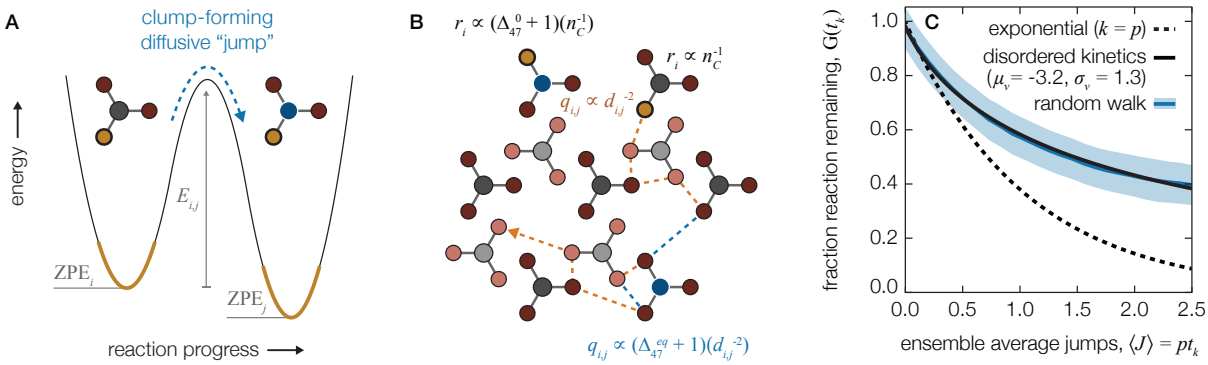

Figure 2: The random walk bond reordering model: (**A**) Potential energy wells for oxygen atoms vibrating about their zero-point energies (ZPE; thick gold lines) in two neighboring CO_3 groups. At the molecular level, diffusion occurs when an oxygen atom "jumps" from one CO_3 group i to a neighboring group j (blue dotted line); a jump requires that the activation energy barrier $E_{i,j}$ is overcome. If an ^{18}O atom (gold circle) jumps to a neighboring ^{13}C-containing group (blue circle), then the ZPE of the resulting clump is lower than that for the initial state and the reaction is thermodynamically favored. (**B**) Conceptual diagram of the model setup. A grid of n_C carbon atoms is created, each with a random probability of being isotopically substituted (blue circles) that is equal to the natural abundance of ^{13}C (assumed $\delta^{13}C = 0$ ‰). An ^{18}O atom (gold circle) is then "seeded" onto the grid; r_i, the probability of initially being associated with carbon atom i, follows a uniform distribution but is increased by a factor of $R^{47,0}/R^{*47}$, the initial Δ_{47} value, for all ^{13}C atoms. At each time step t_k, the ^{18}O atom can "jump" to any of its neighboring carbon atoms with a total probability p such that $p = \sum q_{i,j}$, where $q_{i,j}$ is the probability of jumping to neighboring carbon atom j; $q_{i,j}$ decreases as the square of the distance between the two carbon atoms and is increased by a factor of $R^{47,eq}/R^{*47}$, the equilibrium Δ_{47} value, for all neighboring ^{13}C atoms. An example random walk is shown with the dotted gold (no clump formed at t_k) and blue (clump formed at t_k) trajectory. The random walk process is repeated n_O times for a given carbon grid; uncertainty is determined by recreating the carbon grid n_{iter} times for a total of $n_O \times n_{iter}$ random walks. (**C**) Model results showing $G(t_k)$, the normalized deviation from equilibrium at each time step, as a function of $\langle J \rangle$, the ensemble averaged number of jumps per ^{18}O atom. $\langle J \rangle = pt_k$ is nondimensional time such that $\langle J \rangle = 1$ is the mean life of an exponential decay reaction with rate constant $k = p$ (dotted black line). The model shown here (blue line and shaded region) was initialized with $d_{i,j}$ for calcite (see Fig. 1), $R^{47,0}/R^{*47} = 1.01$, $R^{47,eq}/R^{*47} = 1.0025$, $p = 0.1$, $n_C = 10^4$, $n_O = 10^6$, $n_{iter} = 10^3$, and $n_t = 25$. Also shown is the predicted $G(t_k)$ evolution using the best-fit lognormal disordered kinetics solution (solid black line; Section. 4.1).

uncertainties when extrapolated to geologic *t*-*T* histories.

To obviate the need for *a priori* mechanistic assumptions, here we recast clumped isotope bond reordering as a "disordered" kinetic process whereby solid state C–O isotope exchange occurs as a parallel superposition of pseudo-first-order reactions. We show theoretically that all previously published models represent specific cases of disordered kinetics subject to certain constraints. We then relax these constraints and estimate the distributions of rate coefficients that best fit experimental data using a regularized inverse approach. Resulting rate coefficient distributions are generally well-approximated as lognormal, indicating that underlying E distributions are Gaussian, consistent with the central limit theorem. Finally, we compare our bond reordering predictions to those of previous models and estimate Δ_{47} evolution for examples of geologically relevant heating/cooling histories.

2. Conceptual Framework

To motivate the development of our model, we first conceptualize solid-state bond reordering as a random-walk diffusion process occurring within the crystal lattice (Cole and Chakraborty, 2001; Passey and Henkes, 2012). Although new to mineral isotope studies, disordered kinetics have been successfully applied to similar solid-state reac-

tions; in particular, mineral luminescence decay patterns are shown to result from a distribution "trapping sites" that are analogous to the formation of ^{13}C–^{18}O clumps (Huber, 1985).

For carbonates, ^{18}O diffusion arises when an oxygen atom randomly "jumps" from one CO_3 group i to a neighboring CO_3 group j (Fig. 1; Stolper and Eiler, 2015). Because each atom within a given group vibrates about its zero-point energy (ZPE) such that a jump involves overcoming an activation energy barrier $E_{i,j}$, the probability p of a given atom jumping at any given time is small (Cole and Chakraborty, 2001). Following a harmonic oscillator, we assume $E_{i,j}$ is inversely proportional to $d_{i,j}^2$, the square of the distance between oxygen atoms in neighboring CO_3 groups (Fig. 1). Furthermore, if an ^{18}O atom from a singly substituted CO_3 group jumps to a neighboring ^{13}C-containing CO_3 group, the final ZPE of the newly formed clumped group is lower than that of the initial configuration (i.e., it is thermodynamically favored) due to the nonlinear reduction in ZPE (Fig. 2A; Wang et al., 2004). Lattice defects such as vacancies, interstitials, or Ca^{2+} substitutions likely influence $E_{i,j}$, but their presence is not strictly necessary for diffusion within this framework (Fig. 1; Henkes et al., 2014).

In statistical mechanical terms, this reduction in ZPE leads to an increase in the probability of following a particular diffusion pathway, $q_{i,j}$, when it involves jumping to a neighboring ^{13}C-containing CO_3 group; the magnitude of this increase is proportional to the ZPE difference between singly and doubly substituted groups and, by extension, to the equilibrium Δ_{47} value at a given temperature (Fig. 2B; Schauble et al., 2006). As $T \rightarrow \infty$, the ZPE difference approaches zero and diffusion becomes truly random (i.e., the reduced partition function ratio between singly- and doubly-substituted CO_3 groups approaches unity; Wang et al., 2004), consistent with the requirement that clumped isotopologues are stochastically distributed in the mineral lattice at high T. Critically, this framework differs from the paired reaction-diffusion model in that we do not treat the "pair-to-clump" transition as a separate chemical reaction that follows unique kinetics (k_f in Stolper and Eiler, 2015). Rather, we include this as part of the diffusion process and we increase the probability of this diffusion pathway in a manner predicted by statistical mechanics.

As shown in Fig. 2C, the random-walk diffusion model described here accurately predicts the observed slowdown in Δ_{47} evolution during heating experiments without the need to treat the pair-to-clump transition as a unique chemical reaction or to invoke lattice defects. We interpret this result and predict Δ_{47} evolution on geologic timescales by developing the disordered kinetic model for bond reordering.

3. Methods

3.1. Data compilation

We compiled results from all published experiments designed to derive the kinetics of solid-state $C-O$ bond reordering. This includes Δ_{47} data from 42 experiments using four carbonate minerals: optical and fossil brachiopod

calcite (Passey and Henkes, 2012; Henkes et al., 2014; Stolper and Eiler, 2015; Brenner et al., 2018), aragonite (Chen et al., 2019), dolomite (Lloyd et al., 2018), and the carbonate group within apatite (Stolper and Eiler, 2015). All data were generated using near-identical analytical methods either at the California Institute of Technology (see Passey et al., 2010) or at Johns Hopkins University (see Henkes et al., 2013). To summarize, this included carbonate digestion using a 90 °C common phosphoric acid bath, CO_2 purification by cryogenic and He-carrier gas chromatography, and measurement of m/z 44–49 on a Thermo Scientific MAT 253 isotope ratio mass spectrometer. Reported clumped isotope compositions are calculated as

$$\Delta_{47} = \left[\left(\frac{R^{47}}{R^{*47}} - 1\right) - \left(\frac{R^{46}}{R^{*46}} - 1\right) - \left(\frac{R^{45}}{R^{*45}} - 1\right)\right] \times 1000‰, \quad (1)$$

where R^i is the measured ratio of isotopologue i relative to $^{12}C^{16}O_2$ and R^{*i} is the predicted ratio of isotopologue i relative to $^{12}C^{16}O_2$ if all isotopes were randomly distributed (Affek and Eiler, 2006).

To perform all calculations in a standardized reference frame, we refer to only published data on the "carbon dioxide equilibrium scale" (Dennis et al., 2011) uncorrected for the fractionation factor between 25 °C and 90 °C phosphoric acid reaction (i.e., $CDES_{90}$; Bonifacie et al., 2017). Study-specific fractionation factors were used to uncorrect all data except those presented in Stolper and Eiler (2015); since no fractionation factor was reported for these experiments, a value of 0.092 ‰ was used to match that reported for other data generated in the same laboratory during the same time period (e.g., Bonifacie et al., 2017). Isotopologue reordering reaction progress should be insensitive to the reported Δ_{47} values (i.e., acid or any other standardized correction) so long as equilibrium Δ_{47} is reported in the same reference frame. We thus made no attempt to correct for differences in isotope parameters used between studies.

Assessing model fits requires knowledge of measurement uncertainty. Here, we use Δ_{47} uncertainty reported in each original study without further correction. For samples with replicate measurements, reported uncertainty is the ±1 standard error (s.e.) of all replicates. For samples analyzed only once, reported uncertainty is typically equal to the long-term instrument precision of a suite of standards (Passey et al., 2010; Henkes et al., 2013). In the compiled dataset, uncertainty averages ±0.013 ‰ and never exceeds 0.041 ‰ (n = 355).

All stable isotope data are presented in Table S.1, including: published $\delta^{13}C$, $\delta^{18}O$, and Δ_{47} values; Δ_{47} values after conversion to the $CDES_{90}$ reference frame; and Δ_{47} uncertainty.

3.2. Data analysis

Determining C – O bond reordering progress requires knowledge of $\Delta_{47}^{eq}(T)$, the equilibrium Δ_{47} value at each experimental temperature. We calculate $\Delta_{47}^{eq}(T)$ using the multiple mineralogy high-temperature T vs. $\Delta_{47}^{eq}(T)$ calibration

equation of Bonifacie et al. (2017) (their Eq. 2). However, Lloyd et al. (2018) advocate for the theoretical calibration equation of Schauble et al. (2006) (corrected to $CDES_{90}$) for dolomite reordering experiments since the Bonifacie et al. (2017) calibration over-estimates measured high-temperature dolomite $\Delta_{47}^{eq}(T)$ values by up to 0.015 ‰. For consistency, we retain the Bonifacie et al. (2017) calibration for all calculations performed herein but discuss in Section 5.3 the degree to which this choice influences resulting activation energy estimates.

All calculations were performed using the 'isotopylog' package in Python 3.7 (Hemingway, 2020). Regularized inversion solutions (Section 4.2.1) were determined using the non-negative least squares algorithm in Lawson and Hanson (1995), whereas lognormal rate distribution solutions (Section 4.2.2) and Arrhenius parameters (Section 4.3), including error estimation, were determined using the Levenberg-Marquardt algorithm for non-linear curve fitting with each data point weighted by the inverse of its analytical variance (Marquardt, 1963). Python scripts to generate all figures and tables are included in the supplementary information.

4. Theory

Here, we derive the disordered kinetic model and show that it reproduces Δ_{47} evolution slowdown observed during random-walk diffusion and in carbonate heating experiments (Section 4.1), and we demonstrate that the "pseudo-first-order" (Passey and Henkes, 2012), "transient/equilibrium-defect" (Henkes et al., 2014), and "paired reaction-diffusion" (Stolper and Eiler, 2015) models all represent specific cases of disordered kinetics. We further describe how this framework can inform non-monotonic Δ_{47} evolution, as has been observed in aragonite heating experiments (Chen et al., 2019). We then outline an inversion approach to determine the rate distributions that best fit experimental data, and we show that these distributions are approximately lognormal (Section 4.2). Finally, we estimate the underlying activation energy distributions using an Arrhenius approach (Section 4.3) and show how to calculate Δ_{47} evolution—including uncertainty propagation—over geologically relevant time-temperature histories (Section 4.4). For reference, all mathematical symbols are described in Table S.2.

4.1. Theoretical derivation

Carbonate isotopologue reordering can be written as

$$^{12}C^{16}O_3 + {}^{13}C^{18}O^{16}O_2 \underset{\alpha(T)\kappa(t)}{\overset{\kappa(t)}{\rightleftharpoons}} {}^{13}C^{16}O_3 + {}^{12}C^{18}O^{16}O_2, \tag{2}$$

where $\kappa(t)$ is the apparent rate coefficient of the "order-to-disorder" reaction at time t and $\alpha(T)$ is the temperature-dependent equilibrium constant (Passey and Henkes, 2012). A general feature of all carbonate isotopologue reordering experiments is that $\kappa(t)$ decreases with time, either monotonically (apatite, calcite, dolomite; Passey and Henkes, 2012;

Henkes et al., 2014; Stolper and Eiler, 2015; Brenner et al., 2018; Lloyd et al., 2018) or after early transient features have dissipated (aragonite; Chen et al., 2019).

A decreasing apparent rate coefficient can be shown to result from a superposition of multiple reactions, each following a unique rate coefficient k (Huber, 1985; Ross and Vlad, 1999). This approach is commonly applied to disordered systems such as organic carbon remineralization (Forney and Rothman, 2012a; Hemingway et al., 2017), fossil fuel pyrolysis (Burnham and Braun, 1999), nonlinear chemical kinetics (Ross and Vlad, 1999), and luminescence decay in crystals (Huber, 1985). Here, we suppose that carbonate Δ_{47} evolution during isotopologue reordering similarly follows disordered kinetics. We define the normalized deviation from equilibrium for a subset of material that is associated with a given rate coefficient k at time t as

$$g(k,t) = \frac{\Delta_{47}(k,t) - \Delta_{47}^{\mathrm{eq}}(T)}{\Delta_{47}^{0} - \Delta_{47}^{\mathrm{eq}}(T)}, \tag{3}$$

where $\Delta_{47}(k,t)$ is the Δ_{47} value of material associated with rate k at time t, Δ_{47}^{0} is the measured Δ_{47} value at $t = 0$, and $\Delta_{47}^{\mathrm{eq}}(T)$ is the temperature-dependent equilibrium Δ_{47} value, either measured empirically (e.g., Passey and Henkes, 2012; Bonifacie et al., 2017) or determined theoretically using first-principles estimates of $\alpha(T)$ (Schauble et al., 2006).

Following Passey and Henkes (2012), we show in Appendix A that $g(k,t)$ evolves with time as

$$g(k,t) = e^{-kt}. \tag{4}$$

That is, $g(k,t)$ follows first-order kinetics. We similarly define the normalized deviation from equilibrium for the bulk sample at time t as

$$G(t) = \frac{\Delta_{47}(t) - \Delta_{47}^{\mathrm{eq}}(T)}{\Delta_{47}^{0} - \Delta_{47}^{\mathrm{eq}}(T)}, \tag{5}$$

where $\Delta_{47}(t)$ is the measured Δ_{47} value at time t. $G(t)$ evolves as a superposition of first-order reactions:

$$G(t) = \int_{0}^{\infty} p(k)g(k,t)dk, \tag{6}$$

where $p(k)$ is the fraction of total material initially associated with rate coefficient k such that $p(k) \geq 0$ for all k and

$$\int_{0}^{\infty} p(k) \equiv 1. \tag{7}$$

That is, $p(k)$ forms a probability density function (pdf). Substituting Eq. 4 into Eq. 6 yields

$$G(t) = \int_0^\infty p(k)e^{-kt}dk, \tag{8}$$

which defines the Laplace transform of $p(k)$ (Hansen, 1994; Forney and Rothman, 2012a). Because the superposition of parallel first-order reactions is itself first order, it follows that

$$\frac{dG(t)}{dt} = -\kappa(t)G(t), \tag{9}$$

where $\kappa(t)$ is the apparent rate coefficient at time t (Eq. 1). Combining Eqs. 8 and 9 yields

$$\kappa(t) = \frac{\int_0^\infty kp(k)e^{-kt}dk}{\int_0^\infty p(k)e^{-kt}dk}, \tag{10}$$

which defines the arithmetic mean of k weighted by $p(k)e^{-kt}$. Equation 10 states that small k values become more heavily weighted with increasing t since e^{-kt} approaches zero most rapidly for large k. Put differently, $\kappa(t)$ must decrease with time for any distribution of $p(k)$ other than a single delta function [in which case $\kappa(t)$ is constant; see Section 4.1.1]. The observed decrease in $\kappa(t)$, which prompted the development of the transient/equilibrium-defect (Henkes et al., 2014) and paired reaction-diffusion (Stolper and Eiler, 2015) models, is thus a natural consequence of disordered kinetics. We now demonstrate that Eq. 8 can describe all previous isotopologue reordering models given the right choice of $p(k)$.

4.1.1. Relationship to previous models: Passey and Henkes (2012)

We first consider the "pseudo-first-order" model, which supposes that reordering after some critical time point t_{cr} follows a single first-order reaction with rate constant k_c. This is written mathematically as a delta function, which has the properties

$$\delta(k - k_c) = \begin{cases} \infty, & \text{if } k = k_c \\ 0, & \text{otherwise} \end{cases} \tag{11}$$

and

$$\int_{-\infty}^{\infty} \delta(k - k_c)dk = 1. \tag{12}$$

Reaction progress for $t < t_{\mathrm{cr}}$ is ignored since it is hypothesized to include "transient defects," the loss of which is assumed to be an artifact of experimental heating. We thus define $\tau = t - t_{\mathrm{cr}}$ and $p(k) = \delta(k - k_c)$. Equation 8 becomes

$$\begin{aligned} G(\tau) &= \int_0^\infty \delta(k - k_c) e^{-k\tau} dk, \\ &= e^{-k_c \tau}, \end{aligned} \tag{13}$$

which is identical to governing equation of Passey and Henkes (2012) (their Eq. 3). It can be similarly shown from Eq. 10 that $\kappa(\tau) = k_c$ for all τ, as expected.

4.1.2. Relationship to previous models: Henkes et al. (2014)

Next, we consider the "transient defect/equilibrium defect" model. This is an extension of the pseudo-first-order model that includes transient defect reaction progress when $t < t_{cr}$. Henkes et al. (2014) state that $G(t)$ follows a first-order reaction (Eq. 9) with an apparent rate constant that evolves as (their Eq. A.11)

$$\kappa(t) = k_c + k_d e^{-k_2 t}. \tag{14}$$

Transient defects are assumed to react with rate k_d and anneal with time following a first-order reaction governed by k_2 where $k_2 \sim 1/t_{\mathrm{cr}}$. It can be seen from Eq. 14 that $\kappa(t) = k_c$ when $t \gg t_{\mathrm{cr}}$, as in the pseudo-first-order model.

Comparing Eqs. 10 and 14, it is apparent that the transient defect/equilibrium defect model follows a parallel superposition of first-order reactions with a distribution $p(k)$ that satisfies

$$\frac{\int_0^\infty k p(k) e^{-kt} dk}{\int_0^\infty p(k) e^{-kt} dk} = k_c + k_d e^{-k_2 t}. \tag{15}$$

Finding $p(k)$ involves solving the inverse Laplace transform, which in this case does not conform to a particular function that can be derived analytically (see Section 4.2, below). Nonetheless, as an example, we show the $p(k)$ distribution that satisfies Eq. 15 for optical calcite heated at 425 °C in Fig. S.1.

4.1.3. Relationship to previous models: Stolper and Eiler (2015)

Finally, we consider the "paired reaction-diffusion" model, which treats Δ_{47} evolution as a serial reaction between "clumps", "pairs", and "singletons". Equation 2 can be rewritten as

$$^{12}C^{16}O_3 + {}^{13}C^{18}O^{16}O_2 \underset{\alpha_1(T)\kappa_1(t)}{\overset{\kappa_1(t)}{\rightleftharpoons}} \text{p} \underset{\alpha_{\text{pd}}(T)\kappa_{\text{pd}}(t)}{\overset{\kappa_{\text{pd}}(t)}{\rightleftharpoons}} (^{13}C^{16}O_3)_s + (^{12}C^{18}O^{16}O_2)_s, \quad (16)$$

where p denotes "paired" $^{13}C^{16}O_3$ groups immediately adjacent to $^{12}C^{18}O^{16}O_2$ groups, the subscript "s" denotes "singleton" $^{13}C^{16}O_3$ or $^{12}C^{18}O^{16}O_2$ groups that do not neighbor any other isotopically substituted group, and pd denotes "pair diffusion". As in Stolper and Eiler (2015), we assume each step of the reaction is described by a single unique rate constant $\kappa_1(t) = k_1$ and $\kappa_{\text{pd}}(t) = k_{\text{pd}}$ and equilibrium constant $\alpha_1(T)$ and $\alpha_{\text{pd}}(T)$. Equation 16 describes a system of paired first-order ordinary differential equations.

Two reactions occurring in series can be treated as a superposition of reactions occurring in parallel (Forney and Rothman, 2014). Specifically for this system, we show in Appendix B that $G(t)$ evolves as

$$G(t) = \sum_{i=1}^{2} r(\lambda_i) e^{-\lambda_i t}, \quad (17)$$

where $\lambda_i \propto k_1, k_{\text{pd}}$ are the eigenvalues of the reaction system and and $r(\lambda_i)$ represents $p(k_i)$ projected onto its eigenvectors. The paired reaction-diffusion model is thus a specific case of disordered kinetics. Unlike $p(k)$ however, in general $r(\lambda)$ need not be non-negative since eigenvectors can contain negative entries. Relaxing this constraint can additionally explain non-monotonic $G(t)$ evolution seen in aragonite heating experiments (Chen et al., 2019).

4.1.4. Relaxing the non-negativity constraint

It has recently been observed in isotopologue reordering experiments of aragonite that Δ_{47} does not monotonically approach Δ_{47}^{eq} but rather increases transiently prior to decreasing (Chen et al., 2019). This was interpreted to reflect an initial excess of pairs that rapidly back-react to form clumps on timescales shorter than that of singleton diffusion [i.e., if $\alpha_1(T)\kappa_1(t) \gtrsim \kappa_2(t)$]. This phenomenon is consistent with serial disordered reactions.

We show in Appendix C that, in general,

$$G(t) = \int_0^\infty r(\lambda) e^{-\lambda t} d\lambda, \quad (18)$$

which is the continuous version of Eq. 17 that allows $\kappa_1(t)$ and $\kappa_{\text{pd}}(t)$ to evolve with time. That is, we suppose that

each step in Eq. 16 is itself described by a superposition of first-order reactions that progress at different rates; this is predicted by our random-walk diffusion conceptualization (Fig. 2) and follows from the assumption in Chen et al. (2019) that the activation energy of reaction between a given CO_3 group and any of its neighbors need not be identical. Again recognizing that $r(\lambda)$ is a projection of $p(k)$ onto the eigenvectors of the reaction system, it follows that a $r(\lambda)$ distribution containing significant negative area can lead to transient increases in $G(t)$ with time.

Negative $r(\lambda)$ may be a general feature of serial and feedback systems in which some processes occur at much faster rates than others. Negative $r(\lambda)$ has also been observed in organic matter respiration experiments (Forney and Rothman, 2014) and was interpreted to reflect a lag phase between serial reactions, analogous to the proposed lag prior to the aragonite-to-calcite phase transition observed in Chen et al. (2019).

4.2. Fitting experimental data

Previous models derive rate equations after making assumptions about the system of reordering reactions; for example, that transient defects anneal exponentially (Henkes et al., 2014) or that clumps react with pairs in series (Stolper and Eiler, 2015). This prescribes the form of the $p(k)$ distribution *a priori*. Here, we instead use an inverse approach to find the $p(k)$ distribution that best fits observed data without any *a priori* assumptions about the reordering mechanism; we then compare this solution to a theoretically justified pdf to estimate a functional form of $p(k)$.

4.2.1. Finding the inverse solution

Since we expect k to vary over many orders of magnitude (Passey and Henkes, 2012; Henkes et al., 2014; Stolper and Eiler, 2015; Brenner et al., 2018; Lloyd et al., 2018), we perform a change of variables from k to $\nu = ln(k)$. This facilitates the extraction of underlying activation energy distributions since $E \propto ln(k)$. Probability is conserved, so $p(k)dk = \rho(\nu)d\nu$ and Eq. 8 becomes

$$G(t) = \int_{-\infty}^{\infty} \rho(\nu) e^{-e^{\nu}t} d\nu. \tag{19}$$

As shown in Appendix D, this can be written in matrix from as

$$\mathbf{G} = \mathbf{A}\boldsymbol{\rho}, \tag{20}$$

where $\mathbf{G}$ is the length n_t vector of measured time-series $G(t)$ values, $\boldsymbol{\rho}$ is the length n_ν vector of $\rho(\nu)$ values, and $\mathbf{A}$ is the $n_t \times n_\nu$ Laplace transform operator matrix. Although $\boldsymbol{\rho}$ can be directly calculated as $\boldsymbol{\rho} = \mathbf{A}^{-1}\mathbf{G}$, this solution is highly sensitive to noise at the level of Δ_{47} analytical uncertainty and could lead to negative $\rho(\nu)$ that is mathematically possible but physically unreasonable (Forney and Rothman, 2012b; Hemingway et al., 2017). In mathematical terms, Eq. 20 is ill posed (Hansen, 1994).

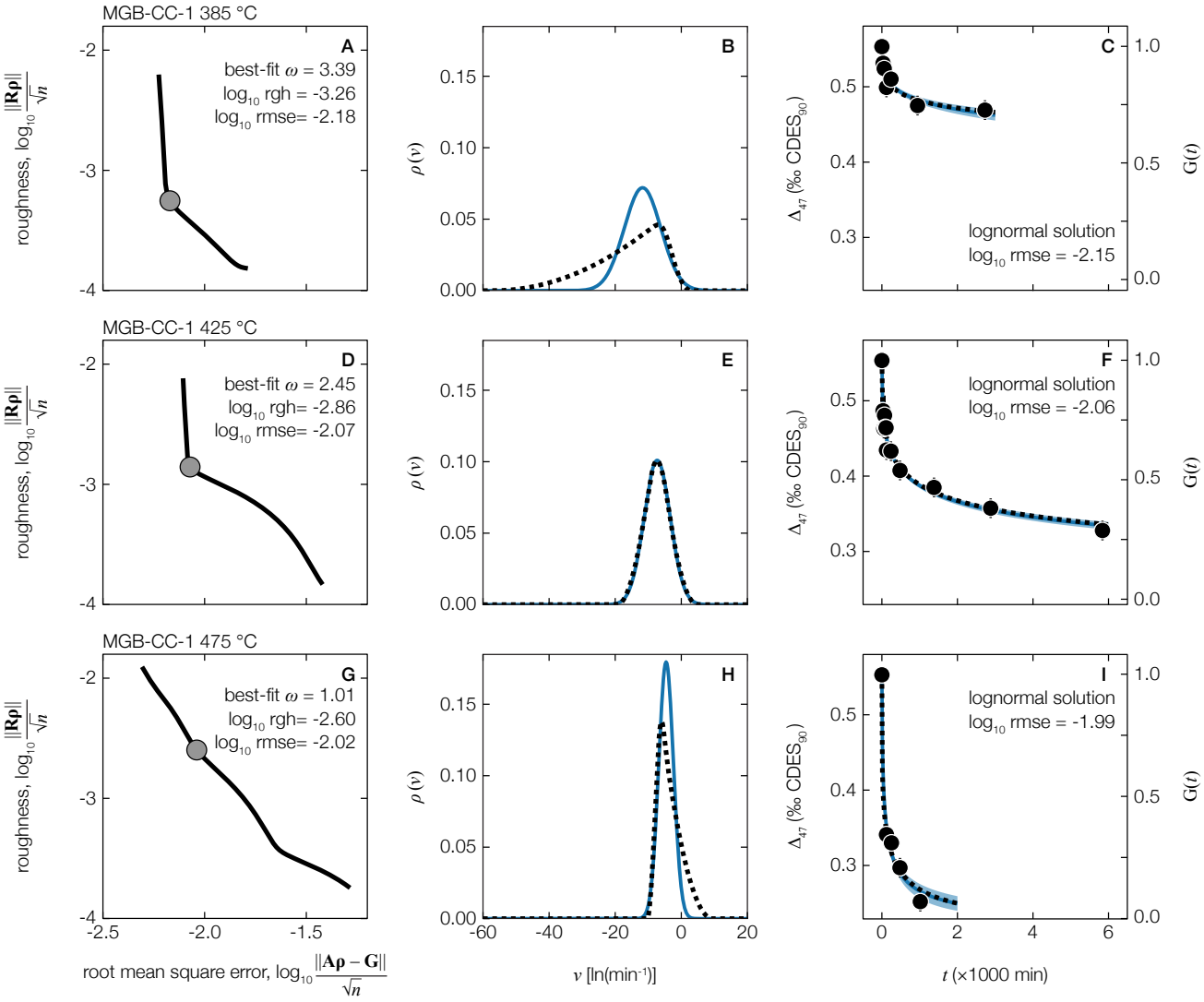

Figure 3: Examples of the disordered kinetic model for optical calcite (MGB-CC-1) isotopologue reordering experiments performed at (**top**) 385, (**middle**) 425, and (**bottom**) 475 °C (data from Passey and Henkes, 2012). Panels **A**, **D**, and **G** show the Tikhonov regularization L-curve for each experiment (solid black line), including the best-fit ω value (gray circle). Panels **B**, **E**, and **H** show the pdf of ν for each experiment, including the best-fit regularized inverse solution (dotted black line) and the lognormal solution (solid blue line). Panels **C**, **F**, and **I** show the measured Δ_{47} values and the modeled Δ_{47} evolution as predicted by the best-fit regularized inverse solution (dotted black line) and the lognormal solution (solid blue line). Shaded blue region is the propagated $\pm 1\sigma$ uncertainty of the lognormal solution. For reference, reaction progress for each experiment is also shown by converting Δ_{47} to $G(t)$. The observed left-skewed regularized inverse solution at lower temperature and right-skewed regularized inverse solution at higher temperature is a general feature of most experiments included in this study (Section 5.1). rgh = roughness; rmse = root mean square error, min = minutes.

We use Tikhonov regularization to find the optimal solution that minimizes $\rho(\nu)$ complexity (determined by the intensity of fluctuations; termed "roughness") while maximizing solution accuracy and ensuring that $\rho(\nu) \geq 0$. Following Forney and Rothman (2012b), we calculate roughness as the $n_\nu \times n_\nu$ bi-diagonal first-derivative operator matrix, $\mathbf{R}$ (Appendix D). The regularized inverse solution is found by including the roughness term in a constrained least

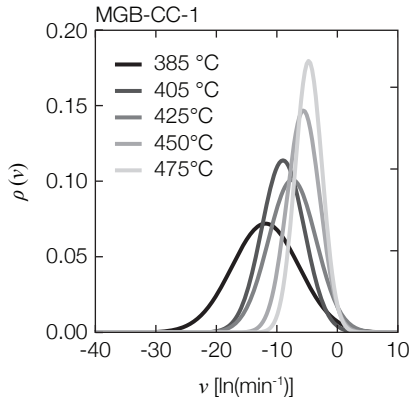

Figure 4: Rate distribution results for optical calcite (MGB-CC-1) isotopologue reordering experiments (data from Passey and Henkes, 2012). Best-fit lognormal rate distributions $\rho(\nu)$ are shown for each experimental temperature (see Table S.3 for distribution statistics). Distributions generally become narrower and shift toward faster rates with increasing temperature, as predicted by Eq. 27 if isotopologue reordering follows an underlying Gaussian distribution of activation energies.

squares problem:

$$\min_{\boldsymbol{\rho}} \|\mathbf{G} - \mathbf{A}\boldsymbol{\rho}\| + \omega\|\mathbf{R}\boldsymbol{\rho}\| \tag{21}$$

subject to the constraints

$$\sum_{j=0}^{n_\nu} \rho_j = 1 \quad \text{and} \quad \rho_j \geq 0 \quad \text{for} \quad j = 1, \ldots, n_\nu, \tag{22}$$

where ω is a scalar that determines how much to weight roughness $\|\mathbf{R}\boldsymbol{\rho}\|$ relative to residual error $\|\mathbf{G} - \mathbf{A}\mathbf{x}\|$. The optimal ω is taken as the point of maximum curvature in a log–log plot of residual error vs. roughness, where each point on the curve is calculated by solving Eq. 21 using ω values that vary over many orders of magnitude (the so-called "L-curve"; Hansen, 1994). From this optimal point, increasing ω greatly increases residual error but has little effect on solution roughness, whereas decreasing ω greatly increases roughness but has little effect on residual error (e.g., Fig. 3A, D, G).

4.2.2. Finding the lognormal solution

For most calcite, dolomite, and apatite samples, the regularized inverse distribution of $\rho(\nu)$ resembles a Gaussian; that is, $p(k)$ is approximately lognormally distributed (e.g., Fig. 3B, E, H). Lognormal $p(k)$ distributions are theoretically justified since they derive naturally from the central limit theorem of multiplicative processes (Montroll and Shlesinger, 1982); they are commonly observed in disordered systems such as organic matter respiration and luminescence decay in minerals (Huber, 1985; Forney and Rothman, 2012a).

To compare with regularized inversion results, we determine the optimal lognormal distribution by setting $\rho(\nu) \sim$

$\mathcal{N}(\mu_\nu, \sigma_\nu)$ and finding μ_ν and σ_ν that best reproduce observed data. That is, we solve

$$\min_{\mu_\nu, \sigma_\nu} \|\mathbf{G} - \mathbf{A}\boldsymbol{\rho}\|, \tag{23}$$

where each entry in $\boldsymbol{\rho}$ is now subject to the constraint

$$\rho(\nu_i) = \frac{1}{\sqrt{2\pi}\sigma_\nu} e^{-(\nu_i - \mu_\nu)^2/2\sigma_\nu^2}, \quad i = 1, \ldots, n_\nu. \tag{24}$$

For all isotopologue reordering experiments, optimal lognormal distributions give $G(t)$ evolution estimates that are statistically indistinguishable from regularized inversion fits and are described by a root mean square error that is well within Δ_{47} analytical uncertainty (e.g., Fig. 3C, F, I).

Resulting lognormal distributions generally shift toward higher μ_ν and lower σ_ν with increasing experimental temperature (Fig. 4). Similar relationships between temperature and bond reordering reaction rates have been observed previously, thus motivating the use of an Arrhenius-like activation energy approach to determine bond reordering temperature dependence (Passey and Henkes, 2012; Henkes et al., 2014; Stolper and Eiler, 2015; Brenner et al., 2018; Lloyd et al., 2018).

4.3. Determining Activation Energies

Because our ultimate goal is to predict isotopologue reordering over geologic timescales, we extract the underlying reaction energetics to predict reaction rates at any arbitrary temperature. As in previous models (Passey and Henkes, 2012; Henkes et al., 2014; Stolper and Eiler, 2015), we suppose that each rate coefficient k follows the Arrhenius equation

$$k(T) = k_0 e^{-E/RT}, \tag{25}$$

where T is temperature, k_0 is the Arrhenius pre-exponential factor, E is the activation energy of bond reordering for material associated $k(T)$, and R is the ideal gas constant. Treating k_0 as constant is strictly inconsistent with transition state theory of chemical reactions, which predicts $k_0 \propto T$ (Eyring, 1935). However, linear dependence of k_0 on T only changes k by a factor of ~ 3 over the temperature range of interest for isotopologue reordering ($\approx 25 - 750$ °C), whereas the exponential term in Eq. 25 varies by many orders of magnitude over this range. Thus, the assumption of constant k_0 negligibly impacts resulting Δ_{47} evolution predictions.

We seek $p(E)$, the pdf of E that leads to measured $\rho(\nu)$ at a given T. If $\rho(\nu) \sim \mathcal{N}(\mu_\nu, \sigma_\nu)$, then we show in

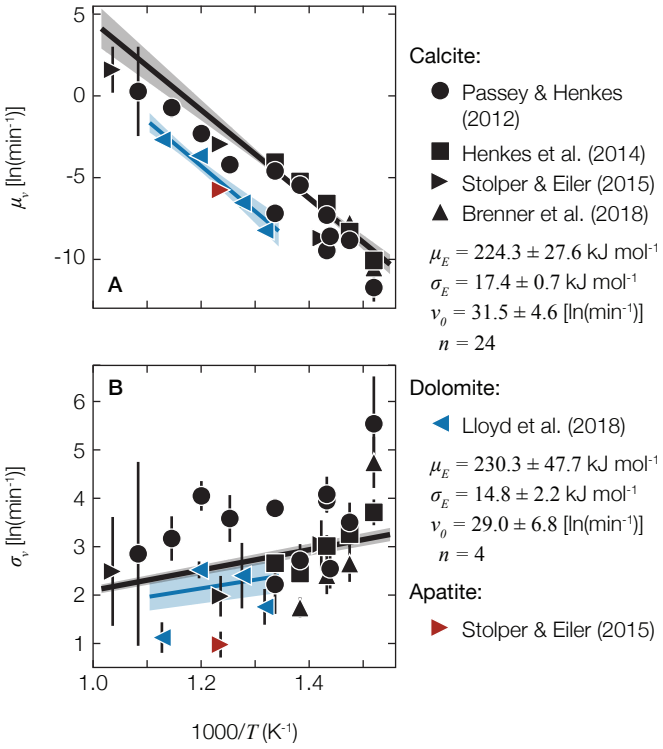

Figure 5: Arrhenius plots showing (**A**) μ_ν and (**B**) σ_ν as a function of inverse experimental temperature. Arrhenius regression best-fit lines calculated using Eq. 27 for calcite (solid black line) and dolomite (solid blue line) are also shown, including $\pm 1\sigma$ uncertainty about each regression line (shaded regions). Experiments exhibiting noisy data [i.e., $\Delta_{47}(t)$ signal-to-noise < 5] or non-monotonic $\Delta_{47}(t)$ evolution were excluded from regressions and thus are not shown here (see Sec. 5.3 and Table S.3).

Appendix E that $p(E) \sim \mathcal{N}(\mu_E, \sigma_E)$ where

$$\begin{aligned} \mu_E &= RT(\nu_0 - \mu_\nu), \\ \sigma_E &= RT\sigma_\nu, \end{aligned} \tag{26}$$

and $\nu_0 = \ln(k_0)$. Rearranging yields

$$\begin{aligned} \mu_\nu &= \nu_0 - \frac{\mu_E}{R}\left(\frac{1}{T}\right), \\ \sigma_\nu &= \frac{\sigma_E}{R}\left(\frac{1}{T}\right). \end{aligned} \tag{27}$$

Equation 27 states that a Gaussian $p(E)$ distribution leads to increasing μ_ν and decreasing σ_ν with increasing temperature, as is observed (Fig. 4). Similar to the approach taken in previous models, we fit $\rho(\nu)$ distributions to a suite of isothermal reordering experiments performed at various temperatures and estimate μ_E and σ_E by linearly regressing μ_ν and σ_ν against $1/T$ (Fig. 5).

4.4. Reordering on geologic timescales

Finally, we seek to predict Δ_{47} evolution for over geologic timescales for any arbitrary t-T history. No analytical solution exists since $G(t)$ does not scale linearly with $\Delta_{47}(t)$ and since $G(t)$ need not decrease monotonically with t (Hemingway et al., 2017); put differently, $\Delta_{47}(t)$ is free to increase or decrease depending on the specific t-T history. We therefore numerically estimate $\Delta_{47}(t)$ evolution following Passey and Henkes (2012). Rewriting Eqs. 5, 19, and 25 in discrete form yields

$$\Delta_{47}(t_i) = \Delta_{47}^{\mathrm{eq}}(T_i) + \left[\Delta_{47}(t_{i-1}) - \Delta_{47}^{\mathrm{eq}}(T_i)\right]\Delta G_i, \tag{28}$$

where

$$\begin{aligned} \Delta G_i &= \left[\sum_{j=1}^{n_E} \mathcal{N}(\mu_E, \sigma_E) \exp\left(-\exp\left[\nu_0 - \frac{E_j}{RT(t_i)}\right]\Delta t\right)\Delta E\right], \\ i &= 2, \ldots, n_t, \\ j &= 1, \ldots, n_E, \end{aligned} \tag{29}$$

Δt and ΔE are the discrete t and E steps, and we impose the initial condition $\Delta_{47}(t_1) = \Delta_{47}^0$. This is written in matrix form as

$$\begin{aligned} \mathbf{\Delta}_{47} &= \phi(\mathbf{t}, \mathbf{T}|\mathbf{y}), \\ \mathbf{y} &= \left[\Delta_{47}^0, \mu_E, \sigma_E, \nu_0\right], \end{aligned} \tag{30}$$

where $\mathbf{t}$ and $\mathbf{T}$ are the length n_t discretized time and temperature vectors, ϕ denotes the function described in Eqs. 28–29 solved at each t_i, T_i given the input parameter values in $\mathbf{y}$, and $\mathbf{\Delta}_{47}$ is the length n_t vector of resulting Δ_{47} values.

We additionally propagate Δ_{47} uncertainty. Uncertainty is derived from each input parameter in $\mathbf{y}$, which contains either analytical error (for Δ_{47}^0) or regression error associated with each Arrhenius plot (for μ_E, σ_E, and ν_0; Fig. 5). We implicitly assume $\Delta_{47}^{\mathrm{eq}}(T_i)$ is perfectly known for all T_i. This is not strictly true; however, $\Delta_{47}^{\mathrm{eq}}(T)$ error is expected to be minor relative to that of each parameter in $\mathbf{y}$ given the strong correlation and low uncertainty in T vs. $\Delta_{47}^{\mathrm{eq}}(T)$ calibration equations (Schauble et al., 2006; Passey and Henkes, 2012; Bonifacie et al., 2017; Lloyd et al., 2018).

Some input parameters are highly correlated—in particular, ν_0 and μ_E (Fig. 5). We account for covariance by propagating error using a Taylor expansion approach (Ku, 1966). Specifically, we calculate Δ_{47} variance at each t_i as

$$\mathbf{\Sigma}_{\mathbf{\Delta}_{47}\mathbf{\Delta}_{47}} = \mathbf{J}\mathbf{\Sigma}_{\mathbf{yy}}\mathbf{J}^T, \tag{31}$$

where $\mathbf{J}$ is the $n_t \times 4$ Jacobian matrix of $\phi(\mathbf{t}, \mathbf{T}|\mathbf{y})$, $\mathbf{\Sigma_{yy}}$ is the 4×4 covariance matrix of $\mathbf{y}$, and $\mathbf{\Sigma}_{\Delta_{47}\Delta_{47}}$ is the resulting $n_t \times n_t$ covariance matrix of predicted Δ_{47} values. The $\pm 1\sigma$ uncertainty in predicted Δ_{47} values is readily determined as $\sqrt{\text{diag}(\mathbf{\Sigma}_{\Delta_{47}\Delta_{47}})}$.

5. Results

5.1. Inverse and lognormal rate distributions

Most calcite, dolomite, and apatite regularized inverse $\rho(\nu)$ distributions are unimodal, symmetric, and lead to predicted $G(t)$ evolution with model-data misfit (root-mean-square error, rmse) that is comparable to analytical uncertainty (Fig. 3, 4; Table S.3). There are two exceptions to this behavior: First, low-temperature experiments ($\lesssim 350$ °C) can result in broad, left-skewed $\rho(\nu)$ distributions (Fig. 3B); this is most apparent for experiments exhibiting small signals and thus analytical signal-to-noise ratios $\lesssim 5$. In extreme cases, left-skewed $\rho(\nu)$ distributions can extend to $\nu \ll -40$, equivalent to rates of $\ll e^{-40}$ min^{-1} at these experimental conditions (Fig. S.2). Material associated with such slow rates would exhibit bond reordering residence times of $\gg 10^{11}$ years and thus remains unreacted over experimental timescales. Second, very high-temperature experiments ($\gtrsim 500$ °C) can lead to right-skewed $\rho(\nu)$ distributions (Fig. 3H) that extend to $\nu \gg 10$, equivalent to rates of $\gg e^{10}$ min^{-1}. Material associated with such fast rates would exhibit bond reordering residence times of $\ll 10^{-5}$ seconds, orders of magnitude shorter than the duration between any two experimental time points and thus not resolvable in any existing dataset.

Both left- and right-skew behaviors are mathematically feasible but physically unconstrained; they emerge when some fraction of material is associated with rates that lead to bond reordering on timescales that lie significantly outside of the analytical time window. We therefore omit from further consideration low-temperature experiments with signal-to-noise ≤ 5 ($n = 4$) as well as high-temperature experiments that reach their $\Delta_{47}^{\text{eq}}(T)$ value prior to the first experimental measurement ($n = 2$), although this choice does not exert a major impact on observed trends. Our final data set includes 24 calcite experiments (spanning 4 studies, 6 calcite types, and 2 pressure/hydration conditions), 1 apatite experiment, and 4 dolomite experiments. Regularized inverse $\rho(\nu)$ distributions of retained experiments exhibit $\log_{10}$ rmse averaging -2.18 ± 0.22 ‰, $\log_{10}$ roughness averaging -2.65 ± 0.43, and $\log_{10}$ ω averaging 0.08 ± 0.54 (mean ± stdev.; $n = 29$); this rmse is comparable to the typical analytical uncertainty of ~0.01 ‰ CDES_{90} (Table S.2).

Lognormal $\rho(\nu)$ distributions exhibit average $\log_{10}$ rmse of -2.08 ± 0.21 ‰ (mean ± stdev.; $n = 29$) and typically result in $G(t)$ evolutions that are nearly identical to those predicted by regularized inverse solutions (Fig. 3). This similarity holds even for experiments exhibiting left- or right-skewed inverse solutions since any $G(t)$ evolution differences resulting from such skew will only manifest outside of the analytical time window. For the entire dataset, $\mu(\nu)$ averages -5.91 ± 3.25 ln(min^{-1}) and exhibits a strong positive correlation with temperature whereas $\sigma(\nu)$ averages

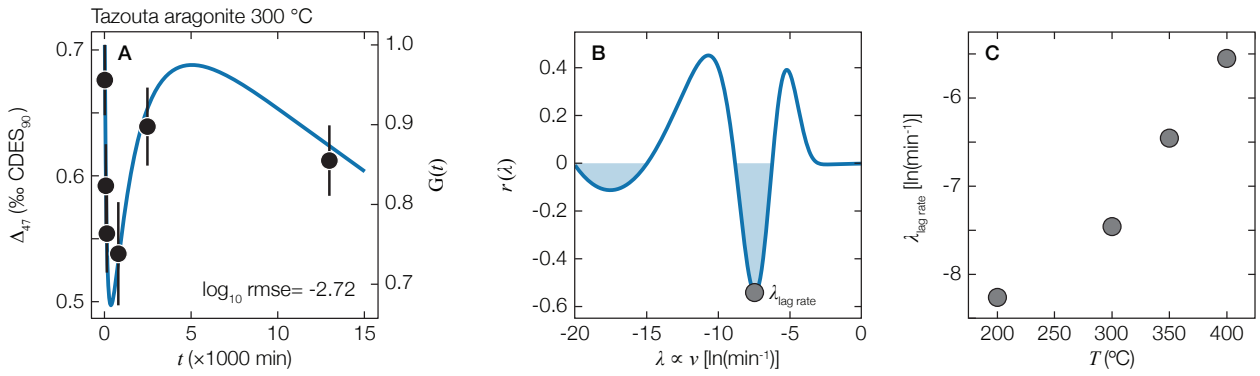

Figure 6: Example of the disordered kinetic model for Tazouta aragonite at 300 °C after relaxing the non-negativity constraint (data from Chen et al., 2019). (**A**) Measured Δ_{47} values and modeled Δ_{47} evolution as predicted by the best-fit (ω = 0.1) regularized inversion $r(\lambda)$ distribution shown in **B**. Importantly, $r(\lambda)$ contains negative area, suggesting aragonite Δ_{47} evolution follows serial disordered kinetics that includes a lag phase operating on the timescale of the λ value at which $r(\lambda)$ reaches its minimum value (here termed $\lambda_{\text{lag rate}}$). (**C**) Predicted $\lambda_{\text{lag rate}}$ as a function of T for a suite of Tazouta aragonite reordering experiments. Predicted $\lambda_{\text{lag rate}}$ increases with T and is roughly equal to the inverse of the time until incipient aragonite-to-calcite transition observed in Chen et al. (2019). For reference, reaction progress is also shown in **A** by converting Δ_{47} to $G(t)$.

2.93 ± 1.01 ln(min^{-1}) and exhibits a strong negative correlation with temperature (Fig. 4-5). Propagated model fit uncertainty is small, with estimated parameter error averaging ±0.35 ln(min^{-1}) for $\mu(\nu)$ and ±0.45 ln(min^{-1}) for $\sigma(\nu)$.

5.1.1. Aragonite inverse rate distributions

Unlike all other carbonate minerals, regularized inverse rate distributions for aragonite heating experiments contain negative area due to the observed transient Δ_{47} increase (Fig. 6). This result prevents the inclusion of aragonite results when determining Gaussian E distributions, since this exercise requires that rate distributions are lognormally distributed (Eq. 27). Rather, negative $r(\lambda)$ implies that aragonite bond reordering follows serial disordered kinetics in which one process is significantly slower than others (i.e., a lag phase; Forney and Rothman, 2014). Observed lag rates increase from $e^{-8.26}$ min^{-1} at 200 °C to $e^{-5.55}$ min^{-1} at 400 °C, indicating a temperature-dependent lag phase (Fig. 6). This timescale is roughly equal to the time until incipient aragonite-to-calcite phase transition observed by Chen et al. (2019), implicating phase change as the cause of Δ_{47} reordering lag. Importantly, this result does not require the inclusion of arbitrary tuning parameters, as has been done previously (d_i in Table 2 of Chen et al., 2019), nor the assumption that the pair-to-clump reaction is chemically distinct from diffusion (Stolper and Eiler, 2015). Rather, rapid initial Δ_{47} decrease followed by a transient Δ_{47} increase is consistent with random-walk diffusion and a transition from aragonite to calcite O–O bond distances (Fig. 1-2).

5.2. Comparison to previous models

Lognormal distributed kientics results in model fits that are comparable to or better than those for both the transient defect/equilibrium model (Henkes et al., 2014) and the paired reaction-diffusion model (Stolper and Eiler, 2015). All

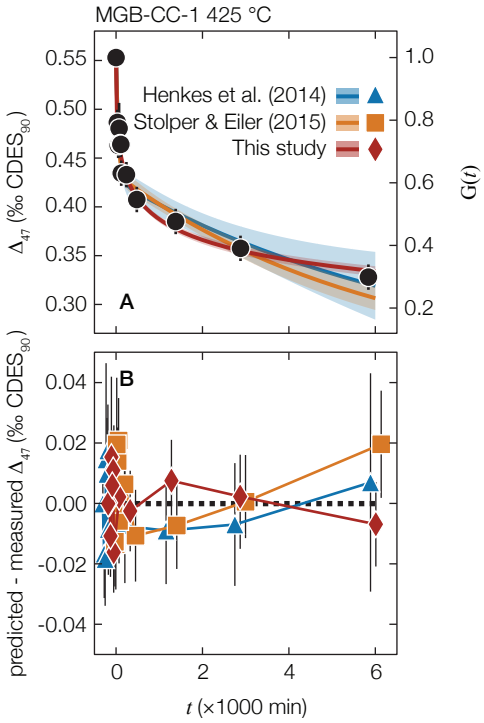

Figure 7: Example model fit comparison for an optical calcite (MGB-CC-1) heating experiment performed at 425 °C showing (**A**) measured and predicted Δ_{47} evolution trends and (**B**) predicted − measured Δ_{47} evolution misfit for each model (data from Passey and Henkes, 2012). Fit statistics for each model are as follows: transient defect/equilibrium defect (blue; Henkes et al., 2014), $\log_{10}$ rmse = −1.94; paired reaction-diffusion (orange; Stolper and Eiler, 2015), $\log_{10}$ rmse = −1.92; lognormal disordered kinetics (red; this study), $\log_{10}$ rmse = −2.06. Shading in **A** represents model parameter $\pm 1\sigma$ uncertainty. Model results in **B** are staggered slightly along the t axis for error bar visual clarity.

models provide similar model-data misfit rmse values. However, estimated $\mu(\nu)$ and $\sigma(\nu)$ uncertainty is considerably less than that predicted for Henkes et al. (2014) and Stolper and Eiler (2015) model parameters, leading to smaller propagated error in $G(t)$ evolution predictions (Fig. 7A).

Furthermore, treating reordering rates as a continuous distribution naturally leads to a gradual slowdown in $G(t)$ evolution with time; in contrast, the "kinked" rate slowdown behavior of previous models results from fitting a finite set of discrete rates to each experiment (3 for the transient defect/equilibrium defect model; 2 for the paired reaction-diffusion model). This difference in gradual vs. kinked rate slowdown leads to slightly divergent model behavior, evidenced by the differences in predicted − measured Δ_{47} evolution between different model types (Fig. 7B). Specifically, both previous models tend to over-predict Δ_{47} at intermediate time points and under-predict Δ_{47} at late time points; in contrast, the lognormal distributed kinetic model exhibits either the opposite behavior or no trend with time. Although these differences are small and statistically insignificant over the timescales of heating experiments considered here, they may become significant if projected over longer experimental timescales.

Table 1: Arrhenius regression activation energy distribution results (Eq. 27) for individual calcite and dolomite sample materials and for the "all calcite" average. Experiments exhibiting noisy data [i.e., $\Delta_{47}(t)$ signal-to-noise < 5] or non-monotonic $\Delta_{47}(t)$ evolution were excluded from these calculations (see Sec. 5.3 and Table S.3). Sample materials are only included here if ≥ 3 experiments were retained after this screening procedure. OC = optical calcite; BC = brachiopod shell calcite; SC = spar calcite; D = dolomite; WHP = wet, high-pressure experiments; n = number of experiments included in Arrhenius regression.

sample	μ_E (kJ mol^{-1})		ν_0 (min^{-1})		σ_E (kJ mol^{-1})		n	data reference
	mean	std. dev.	mean	std. dev.	mean	std. dev.		
Eugui dolomite (D)	230.3	47.7	29.0	6.8	14.8	2.2	4	Lloyd et al. (2018)
MGB-CC-1 (OC)	290.2	27.1	42.7	4.6	20.4	1.8	5	Passey and Henkes (2012)
MGB-CC-1 (OC; WHP)	277.8	40.9	41.2	7.1	13.5	2.7	4	Brenner et al. (2018)
NE-CC-1 (SC)	264.4	16.8	35.6	2.7	24.3	0.8	6	Passey and Henkes (2012)
Mexico calcite (OC)	250.7	13.6	34.2	2.3	15.7	1.7	3	Stolper and Eiler (2015)
WA-CB-13 (BC)	247.4	15.6	35.8	2.6	16.6	0.6	5	Henkes et al. (2014)
All calcite average	**224.3**	**27.6**	**31.5**	**4.6**	**17.4**	**0.7**	**24**	**–**

5.3. Activation energy distributions

Similar to previous observations, disordered kinetic model parameter values scale linearly with $1/T$ following Arrhenius-like behavior (Fig. 5). Combining all calcite samples yields a μ_ν Arrhenius regression described by $\mu_E = 224.3 \pm 27.6$ kJ mol^{-1} and $\nu_0 = 31.5 \pm 4.6$ ln(min^{-1}) and a σ_ν Arrhenius regression described by $\sigma_E = 17.4 \pm 0.7$ kJ mol^{-1} [μ_ν rmse = 1.3 ln(min^{-1}); σ_ν rmse = 0.9 ln(min^{-1}); $n = 24$]. Similarly, dolomite experiments yield a μ_ν Arrhenius regression described by $\mu_E = 230.3 \pm 47.7$ kJ mol^{-1} and $\nu_0 = 29.0 \pm 6.8$ ln(min^{-1}) and a σ_ν Arrhenius regression described by $\sigma_E = 14.8 \pm 2.2$ kJ mol^{-1} [μ_ν rmse = 0.5 ln(min^{-1}); σ_ν rmse = 0.6 ln(min^{-1}); $n = 4$].

When separated into individual experimental materials, calculated μ_E ranges from a minimum of 230.3 ± 47.7 kJ mol^{-1} for Eugui dolomite to a maximum of 290.2 ± 27.1 kJ mol^{-1} for optical calcite sample MGB-CC-1; similarly, σ_E ranges from a minimum of 14.8 ± 2.2 kJ mol^{-1} for Eugui dolomite to a maximum of 24.3 ± 0.8 kJ mol^{-1} for spar calcite sample NE-CC-1 (Table 1). Although all calculated μ_E results are statistically identical (two-tailed t test; $p > 0.05$), the "combined calcite" value appears lower than that for any individual calcite type due to bias caused by differences in the $1/T$ ranges spanned by experiments using different calcite types. In contrast to μ_E, calculated σ_E values exhibit statistically significant differences between sample materials ($p < 0.05$; Table 1), potentially due to differences in trace element contents, ionic impurities, and/or crystallogrpahic defect concentrations (Fig. 1; Henkes et al., 2014; Lloyd et al., 2018).

Arrhenius regression results exhibit a minor dependence on the choice of $\Delta_{47}^{\mathrm{eq}}(T)$ calibration equation (Bonifacie et al., 2017; Lloyd et al., 2018). Specifically, recalculating lognormal disordered kinetic model fits and Arrhenius regression parameters using the $\Delta_{47}^{\mathrm{eq}}(T)$ equation advocated by Lloyd et al. (2018) (their Eq. 4) decreases the "combined calcite" μ_E value to 205.5 ± 31.1 kJ mol^{-1} and leads to slightly higher rmse values but has little impact on ν_0 and σ_E [μ_ν rmse = 1.4 ln(min^{-1}); σ_ν rmse = 1.5 ln(min^{-1}); $n = 24$; Fig. S.3]. In contrast, recalculating dolomite results using

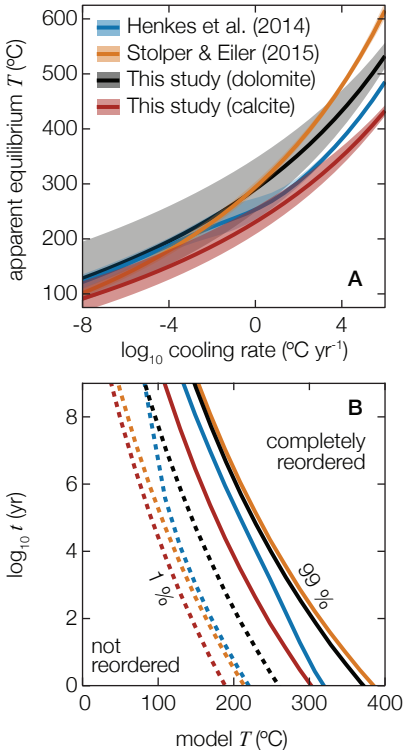

Figure 8: Isotopologue reordering diagnostic plots. (**A**) Apparent equilibrium temperature, $T(\Delta_{47})_{ae}$, for a variety of cooling rates. To generate each line, Δ_{47} is initially in equilibrium at an arbitrarily high temperature, which then decreases linearly at a given rate. $T(\Delta_{47})_{ae}$ at each cooling rate is determined using the calculated apparent equilibrium Δ_{47} value for that rate. (**B**) Time-temperature fields for Δ_{47} preservation. To generate each line, material that is initially described by $T(\Delta_{47})$ = 25 °C is assumed to be instantaneously heated and held at a given temperature; dotted lines indicate the time until incipient (1%) isotopologue reordering, which is conservative and may be below the detection limit given typical precision on natural samples, whereas solid lines indicate the time until complete (99%) isotopologue reordering at that temperature. Colors indicate predictions using the kinetic values for each model as reported in their original publications: blue = transient defect/equilibrium defect (Henkes et al., 2014), orange = paired reaction-diffusion (Stolper and Eiler, 2015), black = dolomite lognormal disordered kinetics (this study), red = calcite lognormal disordered kinetics (this study). Shading in **A** represents model parameter $\pm 1\sigma$ uncertainty.

the Lloyd et al. (2018) $\Delta_{47}^{eq}(T)$ equation increases μ_E to 258.3 ± 43.7 kJ mol^{-1} and σ_E to 20.9 ± 3.4 kJ mol^{-1} [μ_ν rmse = 0.5 ln(min^{-1}); σ_ν rmse = 0.8 ln(min^{-1}); n = 4; Fig. S.3)]. None of these differences in Arrhenius parameters calculated using the Bonifacie et al. (2017) or the Lloyd et al. (2018) $\Delta_{47}^{eq}(T)$ calibration equations is statistically significant (two-tailed t test; $p > 0.05$).

6. Discussion

6.1. Model results, implication, and application

This disordered kinetic model provides a generalizable framework of carbonate isotopologue bond reordering. Importantly, previous models (Henkes et al., 2014; Stolper and Eiler, 2015) can be treated as specific cases of disordered kinetics. The finding that μ_E for the "all calcite average" appears slightly lower than μ_E for dolomite (although within uncertainty) is consistent with the conclusions of Lloyd et al. (2018) (their Fig. 5) and implies that observed

differences between calcite and dolomite from the same metamorphic system are driven, at least in part, by differential isotopologue reordering behavior during the same thermal history. There were not enough heating experiments on carbonate groups in apatite that met our screening criteria to derive μ_E and σ_E values (see Sec. 5.1). We nonetheless find that apatite μ_ν is lower than calcite but identical to dolomite at equivalent experimental temperatures, whereas apatite σ_ν appears to be slightly lower than any observed calcite or dolomite value (Fig. 5). This result is consistent with the original conclusions of Stolper and Eiler (2015) that experimental heating and empirical carbonatite results for apatite are at odds. Differences between calcite and apatite kinetics, and similarities with dolomite, necessitate additional heating experiments and possible model refinements to accommodate exchange with phosphatic oxygen.

Future studies that include independently constrained thermal histories will provide important natural tests of laboratory-derived kinetics. For example, Δ_{47} measurements on carbonatites result in $T(\Delta_{47})$ values far below the canonically known temperatures of crystallization (Dennis and Schrag, 2010). Akin to the concept of closure temperature in thermochronology (Dodson, 1973), this "apparent equilibrium" Δ_{47}-derived temperature, or $T(\Delta_{47})_{\mathrm{ae}}$, has been shown to depend on geologic cooling rate (Passey and Henkes, 2012). While $T(\Delta_{47})_{\mathrm{ae}}$ measurements may provide a useful geospeedometer, cooling rate predictions are sensitive to the choice of bond reordering kinetic model (Fig. 8A). All models predict similar $T(\Delta_{47})_{\mathrm{ae}}$ values of $\approx$ 100 to 200 °C for geologic cooling rates between 10^{-8} and 10^{-4} °C yr^{-1}, broadly consistent with published Δ_{47} measurements of carbonatites and marbles (Dennis and Schrag, 2010; Stolper and Eiler, 2015; Lloyd et al., 2017). Interestingly, this similarity at slow cooling rates includes both dolomite and calcite predictions. However, $T(\Delta_{47})_{\mathrm{ae}}$ values diverge significantly at faster rates. For a given mineral, the disordered kinetic model presented here always predicts lower $T(\Delta_{47})_{\mathrm{ae}}$ values than both previous models—although these differences are statistically insignificant at the slowest cooling rates—and suggests that calcite $T(\Delta_{47})_{\mathrm{ae}} \gtrsim 400$ °C as the result of isotopologue reordering in natural samples at geologic cooling rates should be rare.

The Δ_{47} preservation of low-temperature carbonates such as shells, micritic cements, and carbonate nodules can similarly be evaluated in the context of isotopologue reordering. Such materials have been shown to exhibit high $T(\Delta_{47})$ values without any obvious geochemical alteration to the original mineral (Henkes et al., 2014; Stolper and Eiler, 2015); understanding this phenomenon is critical for screening and omitting altered samples from paleoclimate studies (e.g., Henkes et al., 2018). However, the time-temperature history at which reordering is predicted to occur depends on the choice of kinetic model (Fig. 8B). Specifically, the model presented here conforms to previous limits of Δ_{47} preservation but results in a left-ward shift for both "incipient" (1%) and "complete" (99%) reordering curves. That is, relative to previous models, ours predicts that less time and/or lower temperatures are needed to reach the same degree of alteration and suggests that previous models overestimate the temperatures at which isotopologue reordering is activated. Observed differences between models may be driven in part by our use of a single calcite Arrhenius

regression (Fig. 5) rather than sample-specific (e.g., brachiopod fossil in Henkes et al., 2014) or experiment-specific curves (e.g., hydrothermal reactions in Brenner et al., 2018). When separated by calcite type, our model conforms more closely to predictions of Henkes et al. (2014), particularly for brachiopod shell materials (Fig. S.4).

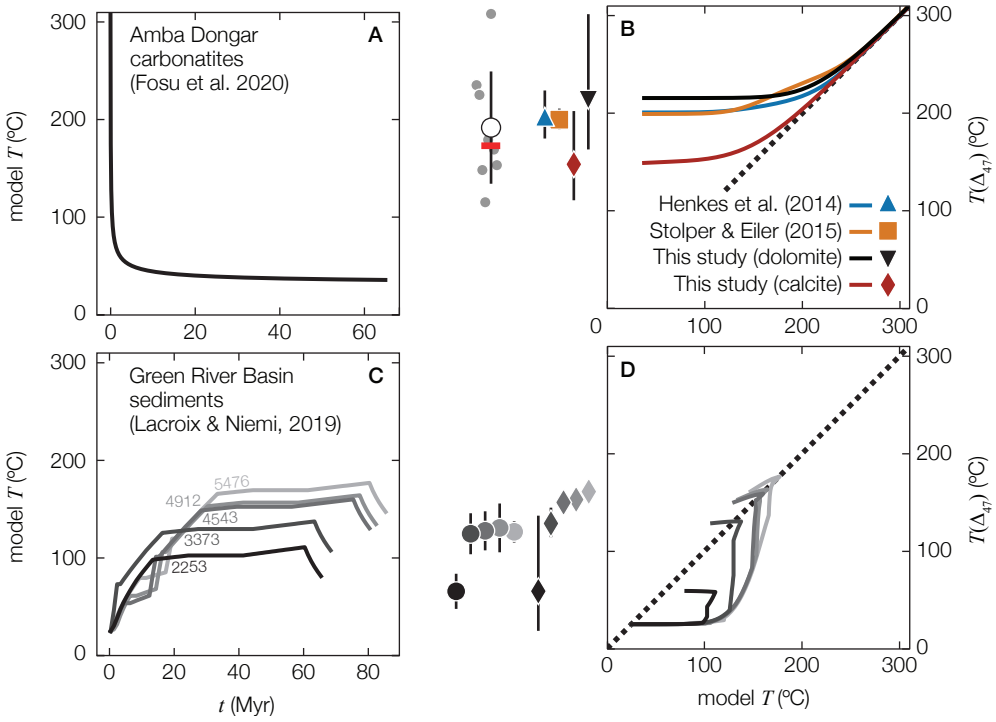

Figure 9: Thermal histories and corresponding model-predicted carbonate $T(\Delta_{47})$ evolution for two geologic examples from the recent literature: (**A**–**B**) a 1D conductive cooling model of the Amba Dongar carbonatite (Fosu et al., 2020, cooling model adapted from Ehlers (2005) for a 550 °C intrusion 1.9 km in diameter that cools by thermal diffusion with 30 °C country rock with a diffusivity of 38 km^2 Ma^{-1}), and (**C**–**D**) modeled thermal history for various sample depths of the Wagon Wheel 1 (WW-1) drill core in the northwestern Green River Basin (Lacroix and Niemi, 2019). Panels **A** and **C** show imposed t–T histories (color-coded by WW-1 core depth in **C**) whereas panels **B** and **D** show reordering model-predicted $T(\Delta_{47})$ plotted against imposed model T. All models in **B** predict closure temperature-like behavior, whereas the T–T pathways predicted by the disordered kinetic model in **D** are more complex and exhibit three distinctive features: (i) the temperature of incipient isotopologue bond reordering, (ii) the rate of approach to equilibrium (shown as a dotted 1 : 1 line), and (iii) the final $T(\Delta_{47})_{ae}$ (shown to the left of the y-axis, including $\pm 1\sigma$ model uncertainty). Colors in **B** indicate predictions using the kinetic values for each model as reported in their original publications. Published $T(\Delta_{47})$ values for each geologic scenario are shown shown as: small gray circles = non-replicated measurements from Amba Dongar (population mean and median as large white circle and red line, respectively; Fosu et al., 2020); large grayscale circles = WW-1 measurements color-coded by core depth, including ±1 s.e. measurement uncertainty.

6.2. Geologic tests

To exemplify how disordered kinetic model predictions might be applied to real geologic systems, we consider thermal histories of two different calcite-containing rocks from the recent literature. The current challenge for any geologic test of clumped isotope bond reordering models is that few natural systems have complete thermal histories that are known independently (e.g., from thermochronology) and have a sufficient number of Δ_{47} measurements for a detailed evaluation of measured versus model-predicted results (exceptions include Shenton et al., 2015; Lloyd et al., 2017; Lawson et al., 2018). Here, we select two Δ_{47} datasets with relatively well-constrained thermal histories to test

model behavior: (i) the Amba Dongar carbonatite complex from the Deccan large igneous province (Gujarat, India; Fig. 9A; Fosu et al., 2020) and (ii) lacustrine limestones from drill core in the Pinedale Anticline of the Green River basin (Wyoming, USA; Fig. 9C; Lacroix and Niemi, 2019).

For the first example, the Amba Dongar thermal history described by Fosu et al. (2020) is a linear 10 °C Myr^{-1} cooling from a 400 °C emplacement temperature at 65 Ma. This cools the intrusion to ambient rock temperatures by 40 Ma, after which there is no additional heating. As noted by Fosu et al. (2020), actual intrusion cooling rates are typically non-linear and asymptotic, so instead we model Amba Dongar carbonatite cooling using a 1D thermal diffusion model whereby the intrusion cools by conduction with the country rock (Fig. 9A; Ehlers, 2005). This cooling pathway could also represent other geologic settings, including contact metamorphism (Lloyd et al., 2017) and heating of sedimentary rocks adjacent to dikes (Finnegan et al., 2011). Given that the starting temperature is equivalent to the warmest laboratory heating experiments (i.e., complete Δ_{47} change within minutes), all kinetic models predict apparent equilibrium temperature behavior. However, each model results in a slightly different $T(\Delta_{47})_{ae}$ value (Fig. 9B). The calcite disordered kinetic model predicts a lower $T(\Delta_{47})_{ae}$ and a shorter interval of departure from equilibrium than both previous models, suggesting Δ_{47} systematics are more "open" during the cooling of igneous and metamorphic rocks than previously thought. This finding is consistent with the mean and median $T(\Delta_{47})$ from the best preserved Amba Dongar calciocarbonatites (B. Fosu, *personal communication*), both of which are lower than previous model predicted $T(\Delta_{47})$. The comparison is limited, however, by outlier high $T(\Delta_{47})$ values that are difficult to interpret without knowing exact sample locations within the intrusion (e.g., samples from the perimeter may have cooled more rapidly than samples from the core).

The second example evaluates bond reordering in deeply buried sedimentary carbonates from the northern Green River Basin using modeled thermal histories for different sample depths of the Wagon Wheel 1 (WW-1) drill core (Fig. 9C, D). Burial temperatures in Lacroix and Niemi (2019) are derived from basin modeling that incorporates stratigraphic thickness, lithology, thermal maturity indices, and geothermal gradients. Unlike conductive cooling of the Amba Dongar complex, modeled WW-1 $T(\Delta_{47})$ exhibits complex and varied features (Fig. 9D). We exclude a direct model-model comparison for this example to highlight depth-dependent patterns (previous bond reordering models were explicitly evaluated by Lacroix and Niemi, 2019). The calcite disordered kinetic model near-perfectly predicts $T(\Delta_{47})$ at WW-1 depths 2253 and 3373 m; this was not the case for all data-model comparisons performed in Lacroix and Niemi (2019). At deeper depths in Fig. 9C and D, our model over-predicts measured $T(\Delta_{47})$ by ≈20 °C; however, Lacroix and Niemi (2019) cite burial model error of 18 °C ($\pm 1\sigma$) during peak heating at 28 to 55 Ma. This allows for the possibility of burial model overestimation of peak temperatures at 4543, 4912, and 5476 m, which would reconcile those apparent data-model discrepancies (Fig. 9D).

6.3. Outlook

The adaptation of disordered kinetic models to describe internal isotopologue reordering in carbonates will enable more targeted future experiments and will provide robust predictions of bond reordering when applied to natural systems. It has been suggested that various carbonate minerals may exhibit unique isotopologue reordering E distributions, possibly driven by inherent differences in metal-oxide bond strength (Lloyd et al., 2018) or O–O distances between neighboring CO_3 groups (Fig. 1). Accurately constraining these distributions may allow for the derivation of independent cooling rates from the same rock in geologic systems that contain multiple carbonate types (Ryb et al., 2017; Lloyd et al., 2017). A mineralogical driver of isotopologue reordering kinetics would predict that one mineralogy can be thermally reset while another, more refractory carbonate may preserve its formation Δ_{47} values after experiencing the same thermal history. Additionally, it has been observed that the same carbonate mineralogy (i.e., calcite) may record different Δ_{47} signatures after burial (Shenton et al., 2015). While the underlying reason(s) for this phenomenon remain elusive, improvements in error propagation developed here (e.g., Fig. 9D) can provide an empirical means to interrogate such trends.

This disordered kinetic framework can be adapted to characterize the reordering kinetics of other, novel mineral isotopologue measurements. For example, sulfate, phosphate, and silicates all contain isotopologue arrangements that include clumps analogous to ^{13}C–^{18}O (e.g., ^{34}S–^{18}O) and/or double heavy isotope substitutions (e.g., ^{18}O–^{18}O) in the oxyanion group; these minerals are likely subject to analogous diffusive bond reordering at elevated temperatures over geologic timescales. Measurement of such isotopologues with sufficient precision to resolve both natural and experimentally induced isotope effects is imminent (Ueno et al., 2019; Neubauer et al., 2020). Furthermore, future carbonate heating experiments should additionally target $^{12}C^{16}O^{18}O_2$ isotopolgue evolution (Δ_{48}) as a complimentary isotopic marker for diffusive C–O bond breakage and reformation in the solid mineral lattice, although analytical signal-to-noise may limit the applicability of this approach (Fiebig et al., 2019). Finally, disordered kinetics may be usefully applied to mineral-pair isotope exchange kinetics and systems where the same elements occupies different intercrystalline sites (e.g., oxyhydroxides; Miller et al., 2020).

7. Conclusion

We show that early, rapid changes in Δ_{47} observed during calcite, dolomite, and apatite laboratory heating experiments arise from random-walk isotope diffusion through the mineral lattice, and we derive a disordered kinetic model to describe these results. This framework can be extended to describe Δ_{47} evolution other minerals, including non-monotonic aragonite evolution (Chen et al., 2019). We show theoretically that two previous models—the transient defect/equilibrium defect model (Sec. 4.1.2; Henkes et al., 2014) and the paired reaction-diffusion model (Sec. 4.1.3;

Stolper and Eiler, 2015)—represent specific cases of disordered kinetics. By fitting published heating experiment Δ_{47} data using an inverse approach, we show that isotopologue reordering rate distributions are approximately lognormal, consistent with the central limit theorem. To extrapolate reordering kinetic model results to geologic scenarios, we determine the underlying Gaussian activation energy distributions using an Arrhenius approach, and we apply these results to two real-world geologic examples. Over geologically reasonable linear cooling rates, all isotopologue reordering models result in $T(\Delta_{47})_{ae} < 600$ °C, with our model indicating that observed $T(\Delta_{47})_{ae} > 400$ °C should be rare for calcite. We also suggest that previous models overestimate the Δ_{47} preservation threshold for calcite paleotemperature archives (e.g., fossil shells). These differences are minor for incipient isotopologue reordering, which conforms with limits established by Henkes et al. (2014), but are larger for nearly complete resetting of Δ_{47}. For complex thermal histories relevant to metamorphic and sedimentary carbonates, we show that the disordered kinetic model yields reductions in error that will be important for empirical tests of model predictions. Lastly, we hypothesize that the disordered kinetic framework should be easily adapted to other current and future mineral isotopologue measurements such as carbonate ^{18}O–^{18}O (Δ_{48}) and sulfate ^{34}S–^{18}O.

Accompanying this paper is an open-source Python package 'isotopylog' (Hemingway, 2020) that allows for model comparisons, incorporation of new isotopologue reordering experiment data (including from new carbonate mineralogies), and the prediction of Δ_{47} during any point of a geologic thermal history.

Acknowledgements

We thank David Johnston, Alison Piasecki, Mark Brandon, and Lars Ehm for helpful discussions; Daniel Stolper for consultation on the paired diffusion model implementation; Benjamin Fosu and Brice Lacroix for access to, and discussion of, geologic data; and the organizers of the Banff Geobiology Society Conference 2019 for stimulating our initial collaborations on this topic. This manuscript benefited greatly from the comments of two anonymous reviewers and Associate Editor Lou Derry. J.D.H. was supported by an NSF Early-Concept Grant for Exploratory Research (EAGER) number EAR1839341 and an American Chemical Society Petroleum Research Fund Grant number 59455-ND2.

Appendix A. Deriving the first-order rate equation

The carbonate isotopologue reordering reaction for material associated with a given rate constant k in a closed system can be written as

$$^{12}C^{16}O_3(k) + {}^{13}C^{18}O^{16}O_2(k) \underset{\alpha(T)k}{\overset{k}{\rightleftharpoons}} {}^{13}C^{16}O_3(k) + {}^{12}C^{18}O^{16}O_2(k), \quad \text{(A.1)}$$

where we have appended each species with (k) to emphasize that this reaction only describes the subset of material associated with rate k. In all subsequent equations, we replace each species with its atomic mass for convenience. This implicitly ignores contributions to each atomic mass by ^{17}O-containing isotoplogues since these are negligible (Wang et al., 2004; Schauble et al., 2006). Following Eq. A.1, the derivative of $^{13}C^{18}O^{16}O_2$ abundance with respect to time can be written as

$$\frac{d[63](k,t)}{dt} = -k[63](k,t)[60](k,t) + \alpha(T)k[61](k,t)[62](k,t), \quad \text{(A.2)}$$

where $[i]$ denotes the fractional abundance of atomic mass i such that $\Sigma_{i=60}^{63}[i] = 1$ (ignoring negligible contributions by other multiply substituted isotopologues; Passey and Henkes, 2012). Similarly following Eq. A.1, we have

$$\alpha(T) = \frac{[60]_{eq}[63]_{eq}}{[61]_{eq}[62]_{eq}}, \quad \text{(A.3)}$$

where the subscript "eq" denotes equilibrium abundance at temperature T; importantly, equilibrium abundances are independent of k. Because $^{12}C^{16}O_3$, $^{13}C^{16}O_3$ and $^{12}C^{18}O^{16}O_2$ are orders-of-magnitude more abundant than $^{13}C^{18}O^{16}O_2$ (Wang et al., 2004; Affek and Eiler, 2006), we assume that changes in the concentrations of these species are negligible and let

$$\begin{aligned} [60](k,t) &= [60]_{eq}, \\ [61](k,t) &= [61]_{eq}, \\ [62](k,t) &= [62]_{eq}. \end{aligned} \quad \text{(A.4)}$$

Combining Eqs. A.2–A.4 yields

$$\frac{d[63](k,t)}{dt} = -k[60]_{\mathrm{eq}}\left\{[63](k,t) - [63]_{\mathrm{eq}}\right\}, \tag{A.5}$$

which is a separable first-order differential equation of the form $x'(t) = a[x(t) + b]$. Because $[60]_{\mathrm{eq}} \approx 1$ (Wang et al., 2004; Affek and Eiler, 2006), we subsume this term into k. The fractional abundance of $^{13}C^{18}O^{16}O_2$ at time t can thus be determined by integrating Eq. A.5 from an initial time $t = 0$:

$$\frac{[63](k,t) - [63]_{\mathrm{eq}}}{[63]_0 - [63]_{\mathrm{eq}}} = e^{-kt}, \tag{A.6}$$

where $[63]_0$ is the fractional abundance of $^{13}C^{18}O^{16}O_2$ at $t = 0$. Similar to equilibrium abundances, initial fractional abundances are independent of k. Equation A.6 is equivalent to (Passey and Henkes, 2012)

$$\frac{\Delta_{63}(k,t) - \Delta_{63}^{\mathrm{eq}}(T)}{\Delta_{63}^{0} - \Delta_{63}^{\mathrm{eq}}(T)} = e^{-kt}, \tag{A.7}$$

where, by analogy to Eq. 1,

$$\Delta_{63} = \left[\left(\frac{R^{63}}{R^{*63}} - 1\right) - \left(\frac{R^{62}}{R^{*62}} - 1\right) - \left(\frac{R^{61}}{R^{*61}} - 1\right)\right] \times 1000‰, \tag{A.8}$$

$R^i = [i]/[60]$, and R^{*i} denotes the R^i value for a stochastic isotopologue distribution (Schauble et al., 2006). Following Guo et al. (2009), we let $\Delta_{63} = \Delta_{47} - \Delta_{47}^{*}$, where the phosphoric acid fractionation factor Δ_{47}^{*} is approximately constant for a given acid digestion temperature. Thus, Eq. A.7 is equal to

$$\frac{\Delta_{47}(k,t) - \Delta_{47}^{\mathrm{eq}}(T)}{\Delta_{47}^{0} - \Delta_{47}^{\mathrm{eq}}(T)} = e^{-kt}. \tag{A.9}$$

Utilizing the definition of $g(k,t)$ from Eq. 3, this can be written as

$$g(k,t) = e^{-kt}. \tag{A.10}$$

Although derivational details differ, this result is identical to that in Appendix A of Passey and Henkes (2012) for bulk $\Delta_{47}(t)$ evolution assuming a single k value.

Appendix B. Relationship between reactions in parallel and in series

Stolper and Eiler (2015) treat the carbonate isotopologue reordering reaction as two processes occurring in series: First, neighboring $^{13}C^{18}O^{16}O_2$ and $^{12}C^{16}O_3$ groups react to form a "pair". Then, paired $^{13}C^{16}O_3$ and $^{12}C^{18}O^{16}O_2$ groups diffuse to form "singletons". Following Eq. 16, the derivative of $^{13}C^{18}O^{16}O_2$ and pair abundances with respect to time is

$$\begin{aligned}\frac{d[63](t)}{dt} &= -k_1[60](t)[63](t) + \alpha_1 k_1[\mathrm{p}](t),\\ \frac{d[\mathrm{p}](t)}{dt} &= k_1[60](t)[63](t) - (\alpha_1 k_1 + k_{\mathrm{pd}})[\mathrm{p}](t)\\ &\quad + \alpha_{\mathrm{pd}} k_{\mathrm{pd}}[61]_s(t)[62]_s(t),\end{aligned} \tag{B.1}$$

where $[i]$ denotes the fractional abundance of atomic mass i and [p] denotes the fractional abundance of pairs such that $\Sigma_{i=60}^{63}[i] + [\mathrm{p}] = 1$. As above, we ignore contributions to each atomic mass by ^{17}O-containing isotopologues (Wang et al., 2004; Schauble et al., 2006). Similarly following Eq. 16, we have

$$\begin{aligned}\alpha_1(T) &= \frac{[60]_{\mathrm{eq}}[63]_{\mathrm{eq}}}{[\mathrm{p}]_{\mathrm{eq}}},\\ \alpha_{\mathrm{pd}}(T) &= \frac{[\mathrm{p}]_{\mathrm{eq}}}{[61]_{s,\mathrm{eq}}[62]_{s,\mathrm{eq}}},\end{aligned} \tag{B.2}$$

where the subscripts "eq" denotes equilibrium abundance at temperature T and the subscript "s" denotes singletons. Because $^{12}C^{16}O_3$, $(^{13}C^{16}O_3)_s$ and $(^{12}C^{18}O^{16}O_2)_s$ are orders-of-magnitude more abundant than pairs and $^{13}C^{18}O^{16}O_2$ (Wang et al., 2004; Affek and Eiler, 2006; Stolper and Eiler, 2015), we again assume that changes in the concentrations of these species are negligible and let

$$\begin{aligned}[60](t) &= [60]_{\mathrm{eq}},\\ [61]_s(t) &= [61]_{s,\,\mathrm{eq}},\\ [62]_s(t) &= [62]_{s,\mathrm{eq}}.\end{aligned} \tag{B.3}$$

Furthermore, we use the fact that $G(t)$ is equivalent to

$$G(t) = \frac{[63](t) - [63]_{\mathrm{eq}}}{[63]_0 - [63]_{\mathrm{eq}}}, \tag{B.4}$$

and we similarly define the reaction progress of pairs as

$$H(t) = \frac{[\mathrm{p}](t) - [\mathrm{p}]_{\mathrm{eq}}}{[63]_0 - [63]_{\mathrm{eq}}}, \tag{B.5}$$

noting that the upper bound of $H(t)$ depends on $[63]_0$ and $[63]_{\mathrm{eq}}$ (i.e., $H(t)$ is not strictly bounded to $[0, 1]$). By substituting Eqs. B.2–B.5 into Eq. B.1, the derivatives of reaction progress with respect to time can be simplified to

$$\begin{aligned} \frac{dG(t)}{dt} &= -k_1 G + \alpha_1 k_1 H, \\ \frac{dH(t)}{dt} &= k_1 G - (\alpha_1 k_1 + k_{\mathrm{pd}}) H. \end{aligned} \tag{B.6}$$

In matrix from, this becomes

$$\frac{d\mathbf{x}(t)}{dt} = \mathbf{B}\mathbf{x}(t), \tag{B.7}$$

where

$$\mathbf{x}(t) = \begin{bmatrix} G(t) \\ H(t) \end{bmatrix}, \quad \mathbf{B} = \begin{bmatrix} -k_1 & \alpha_1 k_1 \\ k_1 & -(\alpha_1 k_1 + k_{\mathrm{pd}}) \end{bmatrix}. \tag{B.8}$$

The solution to Eq. B.8 is found by assuming solutions exist in the form (Forney and Rothman, 2014)

$$\mathbf{x}(t) = \begin{bmatrix} u_1 \\ u_2 \end{bmatrix} e^{-\lambda t}. \tag{B.9}$$

Substituting Eq. B.9 into Eq. B.7 results in the eigenvalue problem

$$-\lambda \begin{bmatrix} u_1 \\ u_2 \end{bmatrix} = \begin{bmatrix} -k_1 & \alpha_1 k_1 \\ k_1 & -(\alpha_1 k_1 + k_{\mathrm{pd}}) \end{bmatrix} \begin{bmatrix} u_1 \\ u_2 \end{bmatrix}, \tag{B.10}$$

where λ must satisfy

$$\det(\mathbf{B} + \lambda \mathbf{I}) = 0, \tag{B.11}$$

and $\mathbf{I}$ is the 2×2 identity matrix. Because $\alpha_1 \gtrsim 1$ and $(k_1 + k_{\mathrm{pd}} + \alpha_1 k_1)^2 > 4 k_1 k_{\mathrm{pd}}$, Eq. B.11 contains two real solutions, λ_1 and λ_2. Substituting these into Eq. B.10 yields the two eigenvectors, $\mathbf{u}_1$ and $\mathbf{u}_2$. The solution to $\mathbf{x}(t)$ is thus a superposition of both exponential decays (Forney and Rothman, 2014)

$$\mathbf{x}(t) = f_1 \mathbf{u}_1 e^{-\lambda_1 t} + f_2 \mathbf{u}_2 e^{-\lambda_2 t}, \tag{B.12}$$

where the weighting factors f_1 and f_2 can be found by substituting the initial conditions G_0 and H_0 at $t = 0$ into Eq. B.12; $G_0 \equiv 1$ by definition whereas H_0 is estimated based on mass spectrometric measurements of $[63]_0$ and known or assumed T vs. $[63]_{eq}$ and T vs. $[p]_{eq}$ relationships (e.g., Eqs. 2 and 17 in Bonifacie et al., 2017; Stolper and Eiler, 2015, respectively). Focusing on $G(t)$, this can be written as

$$G(t) = \sum_{i=1}^{2} r(\lambda_i) e^{-\lambda_i t}, \tag{B.13}$$

where $r(\lambda_i) = f_i u_{i,1}$ can be though of as $p(k_i)$ projected onto the eigenvectors (Forney and Rothman, 2014). Therefore, while Eq. 16 defines two reactions in series, the total isotopologue reordering reaction behaves as two reactions occurring in parallel.

Appendix C. A continuum of paired reaction-diffusion rates

By analogy to Eq. 8, suppose that each step in Eq. 16 is itself described by a parallel superposition of n reactions occurring at various rates. This allows $\kappa_1(t)$ and $\kappa_{pd}(t)$ in Eq. 16 to evolve with time. It follows that

$$G(t) = \sum_{i=0}^{n} p(k_i) g(k_i, t), \quad H(t) = \sum_{i=0}^{n} q(k_i) h(k_i, t), \tag{C.1}$$

where $p(k_i)$ and $q(k_i)$ are the fractional contributions of each k_i to $G(t)$ and $H(t)$, respectively, and

$$\sum_{i=1}^{n} p(k_i) \equiv 1, \quad \sum_{i=1}^{n} q(k_i) \equiv 1. \tag{C.2}$$

Equation B.7 can be rewritten for the fraction of material associated with a given k as

$$\begin{aligned} \frac{dg(k_i, t)}{dt} &= -k_i g(k_i, t) + p(k_i)\alpha_1 \sum_{j=1}^{n} q(k_j) k_j h(k_j, t), \\ \frac{dh(k_i, t)}{dt} &= q(k_i) \sum_{j=1}^{n} p(k_j) k_j g(k_j, t) \\ &\quad - \left(\alpha_1 \sum_{j=1}^{n} p(k_j) k_j + k_i \right) h(k_i, t). \end{aligned} \tag{C.3}$$

Reaction progress again follows Eq. B.8 but with

$$\mathbf{x}(t) = \begin{bmatrix} \mathbf{g}(t) \\ \mathbf{h}(t) \end{bmatrix}, \tag{C.4}$$

where

$$\begin{aligned}\mathbf{g}(t) &= \left[g(k_1,t), g(k_2,t), \ldots, g(k_n,t)\right]^T, \\ \mathbf{h}(t) &= \left[h(k_1,t), h(k_2,t), \ldots, h(k_n,t)\right]^T,\end{aligned} \tag{C.5}$$

and $\mathbf{B}$ is now a $2n \times 2n$ matrix with each row calculated using Eq. C.3. As above, $\mathbf{x}(t)$ can be found by assuming solutions in the form

$$\mathbf{x}(t) = \begin{bmatrix} u_1 \\ u_2 \\ \vdots \\ u_{2n} \end{bmatrix} e^{-\lambda t}. \tag{C.6}$$

There now exist $2n$ solutions with unique eigenvalues and eigenvectors. The overall solution is again a superposition of all exponential decays (Forney and Rothman, 2014) calculated as

$$\mathbf{x}(t) = \mathbf{U} e^{-\mathbf{\Lambda} t} \mathbf{f}, \tag{C.7}$$

where $\mathbf{U}$ is the $2n \times 2n$ matrix of eigenvectors, e is the matrix exponential, $\mathbf{\Lambda}$ is the $2n \times 2n$ diagonal matrix of eigenvalues, and $\mathbf{f}$ is the vector of weighting factors. As above, $\mathbf{f}$ is found by substituting the initial conditions into Eq. C.7:

$$\mathbf{f} = \mathbf{U}^{-1} \mathbf{x}_0, \tag{C.8}$$

where

$$\mathbf{x}_0 = \begin{bmatrix} \mathbf{g}_0 \\ \mathbf{h}_0 \end{bmatrix}, \tag{C.9}$$

and

$$\begin{aligned}\mathbf{g}_0 &= G_0 \left[p(k_1), p(k_2), \ldots, p(k_n)\right]^T, \\ \mathbf{h}_0 &= H_0 \left[q(k_1), q(k_2), \ldots, q(k_n)\right]^T.\end{aligned} \tag{C.10}$$

G_0 and H_0 are calculated as in Appendix B. Each entry in $\mathbf{x}(t)$ is thus equal to

$$x_i(t) = f_i \sum_{j=1}^{2n} u_{j,i} e^{-\lambda_i t}. \tag{C.11}$$

Again focusing solely on $G(t)$ and recalling that the first n rows of $\mathbf{x}(t)$ correspond to each $g(k_i, t)$, Eqs. C.1 and C.11 can be combined to give

$$G(t) = \sum_{i=1}^{n} r(\lambda_i) e^{-\lambda_i t}, \tag{C.12}$$

where

$$r(\lambda_i) = p(k_i) f_i \sum_{j=1}^{2n} u_{j,i}. \tag{C.13}$$

Equation C.12 is readily written in continuous form as

$$G(t) = \int_0^{\infty} r(\lambda) e^{-\lambda t}. \tag{C.14}$$

Similar to the 2-component case (Appendix B), a system of two reactions in series—each of which following a parallel superposition of first-order reactions at different rates—behaves itself as a superposition of reactions occurring in parallel. A unique feature of serial reactions is that each $r(\lambda_i)$ can be negative since this represents $p(k)$ projected onto eigenvectors whose entries need not be positive (Eq. C.13).

Appendix D. Solving the inverse Laplace transform

To numerically estimate $\rho(\nu)$, we first discretize t and $G(t)$ into vectors $\mathbf{t}$ and $\mathbf{G}$ containing n_t nodes such that each node corresponds to the time of each Δ_{47} measurement (Forney and Rothman, 2012b; Hemingway et al., 2017). Importantly, this does not require a uniform time step since Δ_{47} reordering experiments are rarely uniformly distributed in time. We similarly discretize ν into a uniformly spaced vector $\boldsymbol{\nu}$ containing n_ν nodes such that

$$\Delta\nu = \frac{\nu_{\max} - \nu_{\min}}{n_\nu}, \tag{D.1}$$

where we let $\nu_{\min} = -60$ and $\nu_{\max} = 20$ based on published data (Passey and Henkes, 2012; Henkes et al., 2014; Stolper and Eiler, 2015; Brenner et al., 2018; Lloyd et al., 2018; Chen et al., 2019).

Equation 19 can be separated into two components: (i) $\rho(\nu)$ and (ii) the Laplace transform operator $e^{-e^{\nu}t}$. We discretize the Laplace transform operator into a $n_t \times n_{nu}$ matrix $\mathbf{A}$ such that

$$\begin{aligned} A_{i,j} &= \exp\left[-\exp\left(\nu_j\right) t_i\right] \Delta\nu, \\ i &= 1, \ldots, n_t, \\ j &= 1, \ldots, n_\nu. \end{aligned} \tag{D.2}$$

Finally, we define $\boldsymbol{\rho}$ to be the unknown, discretized vector of $\rho(\nu)$ such that

$$\rho_j = \frac{1}{\Delta\nu}\int_{\nu_j-\frac{1}{2}\Delta\nu}^{\nu_j+\frac{1}{2}\Delta\nu} \rho(\nu)d\nu, \quad j = 1, \ldots, n_\nu. \tag{D.3}$$

Our model can thus be written in matrix form as

$$\mathbf{G} = \mathbf{A}\boldsymbol{\rho}. \tag{D.4}$$

To find a "smoothed" solution using Tikhonov regularization, we additionally calculate the bi-diagonal first-derivative operator matrix, $\mathbf{R}$. That is, we let

$$\left\|\frac{d\rho(\nu)}{d\nu}\right\| = \left[\sum_{j=2}^{n_\nu-1}\left(\frac{\rho_{j+1}-\rho_j}{\Delta\nu}\right)^2\right]^{\frac{1}{2}} \equiv \|\mathbf{R}\boldsymbol{\rho}\|, \tag{D.5}$$

where the first and last rows of $\mathbf{R}$ are set to $[1 \quad \mathbf{0}]$ and $[\mathbf{0} \quad -1]$, respectively, and $\mathbf{0}$ is the zero vector of length $n_\nu - 1$. This forces the constraint that $\boldsymbol{\rho} = 0$ outside of the range $\nu_{\min} < \nu < \nu_{\max}$ (Forney and Rothman, 2012b).

Appendix E. Deriving $p(E)$ from $\rho(\nu)$

Suppose $\rho(\nu) \sim \mathcal{N}(\mu_\nu, \sigma_\nu)$ and $\nu = \nu_0 - E/RT$, then the pdf of E can be readily calculated by change of variables. That is,

$$\begin{aligned} p(E) &= \rho\{\nu(E)\}\left|\frac{d\nu}{dE}\right|, \\ &= \left(\frac{1}{\sqrt{2\pi}\sigma_\nu}\exp\left[-\frac{(\nu_0 - \frac{E}{RT} - \mu_\nu)^2}{2\sigma_\nu^2}\right]\right)\left|-\frac{1}{RT}\right|. \end{aligned} \tag{E.1}$$

If we let

$$\begin{aligned} \mu_E &= RT(\nu_0 - \mu_\nu), \\ \sigma_E &= RT\sigma_\nu, \end{aligned} \tag{E.2}$$

then this simplifies to

$$p(E) = \frac{1}{\sqrt{2\pi}\sigma_E}\exp\left[-\frac{(E-\mu_E)^2}{2\sigma_E^2}\right], \tag{E.3}$$

which defines a normal distribution with mean μ_E and standard deviation σ_E.

Appendix F. Supplementary data and figures

Supplementary data and figures associated with this article can be found in the online version at http://xxxxxx.

References

Affek, H.P., Eiler, J.M., 2006. Abundance of mass 47 CO_2 in urban air, car exhaust, and human breath. Geochimica et Cosmochimica Acta 70, 1–12.

Bonifacie, M., Calmels, D., Eiler, J.M., Horita, J., Chaduteau, C., Vasconcelos, C., Agrinier, P., Katz, A., Passey, B.H., Ferry, J.M., Bourrand, J.J., 2017. Calibration of the dolomite clumped isotope thermometer from 25 to 350°C, and implications for a universal calibration for all (Ca, Mg, Fe)CO_3 carbonates. Geochimica et Cosmochimica Acta 200, 255–279.

Brenner, D.C., Passey, B.H., Stolper, D.A., 2018. Influence of water on clumped-isotope bond reordering kinetics in calcite. Geochimica et Cosmochimica Acta 224, 42–63.

Burnham, A.K., Braun, R.L., 1999. Global kinetic analysis of complex materials. Energy & Fuels 13, 1–22.

Chen, S., Ryb, U., Piasecki, A.M., Lloyd, M.K., Baker, M.B., Eiler, J.M., 2019. Mechanism of solid-state clumped isotope reordering in carbonate minerals from aragonite heating experiments. Geochimica et Cosmochimica Acta 258, 156–173.

Cole, D.R., Chakraborty, S., 2001. Rates and mechanisms of isotopic exchange. Reviews in Mineralogy & Geochemistry 43, 83–223.

De Villiers, J.P., 1971. Crystal structures of aragonite, strontianite, and witherite. American Mineralogist 56, 758–767.

Dennis, K.J., Affek, H.P., Passey, B.H., Schrag, D.P., Eiler, J.M., 2011. Defining an absolute reference frame for 'clumped' isotope studies of CO_2. Geochimica et Cosmochimica Acta 75, 7117–7131.

Dennis, K.J., Schrag, D.P., 2010. Clumped isotope thermometry of carbonatites as an indicator of diagenetic alteration. Geochimica et Cosmochimica Acta 74, 4110–4122.

Dodson, M.H., 1973. Closure temperature in cooling geochronological and petrological systems. Contributions to Mineralogy and Petrology 40, 259–274.

Ehlers, T.A., 2005. Crustal thermal processes and the interpretation of thermochronometer data. Reviews in Mineralogy and Geochemistry 58, 315–350.

Eiler, J.M., 2011. Paleoclimate reconstruction using carbonate clumped isotope thermometry. Quaternary Science Reviews 30, 3575–3588.

Eyring, H., 1935. The activated complex in chemical reactions. Journal of Chemical Physics 3, 107–115.

Fiebig, J., Bajnai, D., Löffler, N., Methner, K., Krsnik, E., Mulch, A., Hofmann, S., 2019. Combined high-precision Δ_{48} and Δ_{47} analysis of carbonates. Chemical Geology 522, 186–191.

Finnegan, S., Bergmann, K., Eiler, J.M., Jones, D.S., Fike, D.A., Eisenman, I., Hughes, N.C., Tripati, A.K., Fischer, W.W., 2011. The magnitude and duration of late ordovician–early silurian glaciation. Science 331, 903–906.

Forney, D.C., Rothman, D.H., 2012a. Common structure in the heterogeneity of plant-matter decay. Journal of the Royal Society Interface 9, 2255–2267.

Forney, D.C., Rothman, D.H., 2012b. Inverse method for estimating respiration rates from decay time series. Biogeosciences 9, 3601–3612.

Forney, D.C., Rothman, D.H., 2014. Carbon transit through degradation networks. Ecological Monographs 84, 109–129.

Fosu, B.R., Ghosh, P., Viladkar, S.G., 2020. Clumped isotope geochemistry of carbonatites in the north-western deccan igneous province: Aspects of evolution, post-depositional alteration and mineralisation. Geochimica et Cosmochimica Acta 274, 118–135.

Guo, W., Mosenfelder, J.L., Goddard III, W.A., Eiler, J.M., 2009. Isotopic fractionations associated with phosphoric acid digestion of carbonate minerals: Insights from first-principles theoretical modeling and clumped isotope measurements. Geochimica et Cosmochimica Acta 73, 7203–7225.

Hansen, P.C., 1994. Regularization tools: a matlab package for analysis and solution of discrete ill-posed problems. Numerical Algorithms 6, 1–35.

Hemingway, J.D., 2020. *isotopylog*: Open-source tools for clumped isotope kinetic data analysis, 2020-. URL: `http://pypi.python.org/pypi/isotopylog`.

Hemingway, J.D., Rothman, D.H., Rosengard, S.Z., Galy, V.V., 2017. Technical note: An inverse method to relate organic carbon reactivity to isotope composition from serial oxidation. Biogeosciences 14, 5099–5114.

Henkes, G.A., Passey, B.H., Grossman, E.L., Shenton, B.J., Pérez-Huerta, A., Yancey, T.E., 2014. Temperature limits for preservation of primary calcite clumped isotope paleotemperatures. Geochimica et Cosmochimica Acta 139, 362–382.

Henkes, G.A., Passey, B.H., Grossman, E.L., Shenton, B.J., Yancey, T.E., Pérez-Huerta, A., 2018. Temperature evolution and the oxygen isotope composition of phanerozoic oceans from carbonate clumped isotope thermometry. Earth and Planetary Science Letters 490, 40–50.

Henkes, G.A., Passey, B.H., Wanamaker Jr, A.D., Grossman, E.L., Ambrose Jr, W.G., Carroll, M.L., 2013. Carbonate clumped isotope compositions of modern marine mollusk and brachiopod shells. Geochimica et Cosmochimica Acta 106, 307–325.

Huber, D., 1985. Statistical model for stretched exponential relaxation in macroscopic systems. Physical Review B 31, 6070–6071.

Ku, H.H., 1966. Notes on the use of propagation of error formulas. Journal of Research of the National Bureau of Standards 70, 263–273.

Lacroix, B., Niemi, N.A., 2019. Investigating the effect of burial histories on the clumped isotope thermometer: an example from the green river and washakie basins, wyoming. Geochimica et Cosmochimica Acta 247, 40–58.

Lawson, C.L., Hanson, R.J., 1995. Solving least squares problems. volume 15. Siam.

Lawson, M., Shenton, B.J., Stolper, D.A., Eiler, J.M., Rasbury, E.T., Becker, T.P., Phillips-Lander, C.M., Buono, A.S., Becker, S.P., Pottorf, R., Gray, G.G., Yurewicz, D., Gournay, J., 2018. Deciphering the diagenetic history of the el abra formation of eastern mexico using reordered clumped isotope temperatures and u-pb dating. GSA Bulletin 130, 617–629.

Lloyd, M.K., Eiler, J.M., Nabelek, P.I., 2017. Clumped isotope thermometry of calcite and dolomite in a contact metamorphic environment. Geochimica et Cosmochimica Acta 197, 323–344.

Lloyd, M.K., Ryb, U., Eiler, J.M., 2018. Experimental calibration of clumped isotope reordering in dolomite. Geochimica et Cosmochimica Acta 242, 1–20.

Markgraf, S.A., Reeder, R.J., 1985. High-temperature structure refinements of calcite and magnesite. American Mineralogist 70, 590–600.

Marquardt, D.W., 1963. An algorithm for least-squares estimation of nonlinear parameters. Journal of the society for Industrial and Applied Mathematics 11, 431–441.

Miller, H.B., Farley, K.A., Vasconcelos, P.M., Mostert, A., Eiler, J.M., 2020. Intracrystalline site preference of oxygen isotopes in goethite: A single-mineral paleothermometer. Earth and Planetary Science Letters 539, 116237.

Montroll, E.W., Shlesinger, M.F., 1982. On $1/f$ noise and other distributions with long tails. Proceedings of the National Academy of Sciences 79, 3380–3383.

Neubauer, C., Crémière, A., Wang, X.T., Thiagarajan, N., Sessions, A.L., Adkins, J.F., Dalleska, N.F., Turchyn, A.V., Clegg, J.A., Moradian, A., Sweredoski, M.J., Garbis, S.D., Eiler, J.M., 2020. Stable isotope analysis of intact oxyanions using electrospray quadrupole-orbitrap mass spectrometry. Analytical Chemistry 92, 3077–3085.

Passey, B.H., Henkes, G.A., 2012. Carbonate clumped isotope bond reordering and geospeedometry. Earth and Planetary Science Letters 351, 223–236.

Passey, B.H., Levin, N.E., Cerling, T.E., Brown, F.H., Eiler, J.M., 2010. High-temperature environments of human evolution in east africa based on bond ordering in paleosol carbonates. Proceedings of the National Academy of Sciences 107, 11245–11249.

Ross, J., Vlad, M.O., 1999. Nonlinear kinetics and new approaches to complex reaction mechanisms. Annual Reviews of Physical Chemistry 50, 51–78.

Ryb, U., Eiler, J.M., 2018. Oxygen isotope composition of the phanerozoic ocean and a possible solution to the dolomite problem. Proceedings of

733 the National Academy of Sciences 115, 6602–6607.
734 Ryb, U., Lloyd, M., Stolper, D., Eiler, J., 2017. The clumped-isotope geochemistry of exhumed marbles from naxos, greece. Earth and Planetary
735 Science Letters 470, 1–12.
736 Schauble, E.A., Ghosh, P., Eiler, J.M., 2006. Preferential formation of ^{13}C–^{18}O bonds in carbonate minerals, estimated using first-principles lattice
737 dynamics. Geochimica et Cosmochimica Acta 70, 2510–2529.
738 Shenton, B.J., Grossman, E.L., Passey, B.H., Henkes, G.A., Becker, T.P., Laya, J.C., Perez-Huerta, A., Becker, S.P., Lawson, M., 2015. Clumped
739 isotope thermometry in deeply buried sedimentary carbonates: The effects of bond reordering and recrystallization. GSA Bulletin 127, 1036–
740 1051.
741 Stolper, D.A., Eiler, J.M., 2015. The kinetics of solid-state isotope-exchange reactions for clumped isotopes: A study of inorganic calcites and
742 apatites from natural and experimental samples. American Journal of Science 315, 363–411.
743 Ueno, Y., Katsuta, T., Ishimaru, T., Yoshida, N., 2019. A new method for measuring ^{34}S–^{18}O clumping in sulfate, in: Goldschmidt Conference
744 Abstracts.
745 Wang, Z., Schauble, E.A., Eiler, J.M., 2004. Equilibrium thermodynamics of multiply substituted isotopologues of molecular gases. Geochimica
746 et Cosmochimica Acta 68, 4779–4797.

Table S.1: All heating experiment metadata (sample ID, mineralogy, time, temperature, reference) and stable isotope data ($\delta^{13}C$, $\delta^{18}O$, Δ_{47}, Δ_{47} uncertainty) used in this study. Where applicable, Δ_{47} values are presented both in their original reference frame as well as in the $CDES_{90}$ reference frame.

Table S.2: Descriptions of all mathematical symbols used throughout this study.

Table S.3: Resulting statistics of regularized inverse (rmse, roughness norm, ω) and lognormal (rmse, μ_ν, σ_ν) model fits for all heating experiments used in this study. The non-negativity constraint was relaxed for aragonite experiments [i.e., $r(\lambda)$ was fit]; thus, only regularized inverse model fit statistics are included for these experiments.

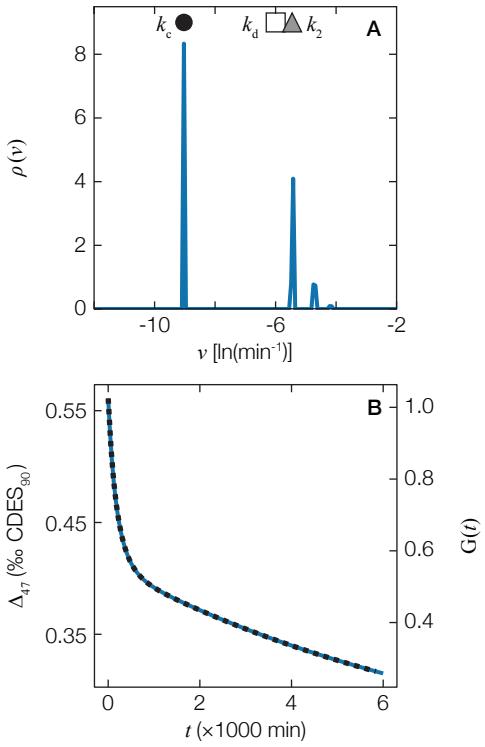

Figure S.1: Example demonstrating that the "transient defect/equilibrium defect" model (Henkes et al., 2014) is consistent with disordered kinetics. Henkes et al. (2014) k values for the model fit to an optical calcite (MGB-CC-1) isotopologue reordering experiment at 425 °C [symbols in **A**; in Henkes et al. (2014) notation; data from their Table B2] were used to generate a Δ_{47} evolution trajectory (dotted black line in **B**). The inverse Laplace transform was then determined from this trajectory, leading to the pdf of ν in **A** and the corresponding forward-modeled Δ_{47} trajectory in **B** (solid blue lines). Both Δ_{47} trajectories are identical, demonstrating that the Henkes et al. (2014) model is perfectly recreated by disordered kinetics. For reference, reaction progress is also shown by converting Δ_{47} to $G(t)$.

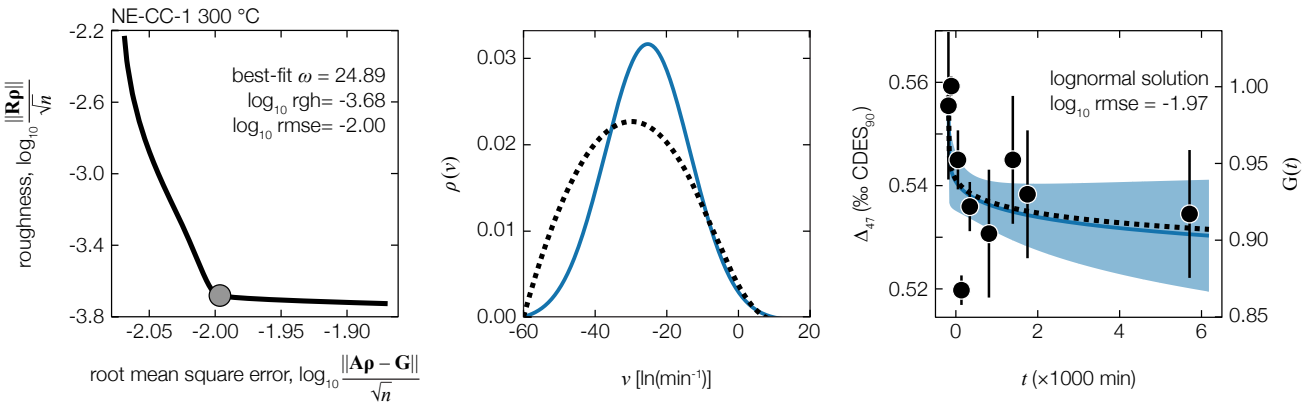

Figure S.2: Same as Fig. 3, but calculated using the spar calcite (NE-CC-1) isotopologue reordering experiment performed at 300 °C (data from Passey and Henkes, 2012). (**A**) Tikhonov regularization L-curve (solid black line), including the best-fit ω value (gray circle). (**B**) pdf of ν, including the best-fit regularized inverse solution (dotted black line) and the lognormal solution (solid blue line). (**C**) measured Δ_{47} values and the modeled Δ_{47} evolution as predicted by the best-fit regularized inverse solution (dotted black line) and the lognormal solution (solid blue line). Shaded blue region is the propagated $\pm 1\sigma$ uncertainty of the lognormal solution. For reference, reaction progress is also shown by converting Δ_{47} to $G(t)$. The model fit is poor for this experiment due to the low analytical signal-to-noise ratio, leading to large model uncertainty and an overly broad, left-skewed inverse solution for $\rho(\nu)$; as such, this experiment was omitted from the final dataset. rgh = roughness; rmse = root mean square error, min = minutes.

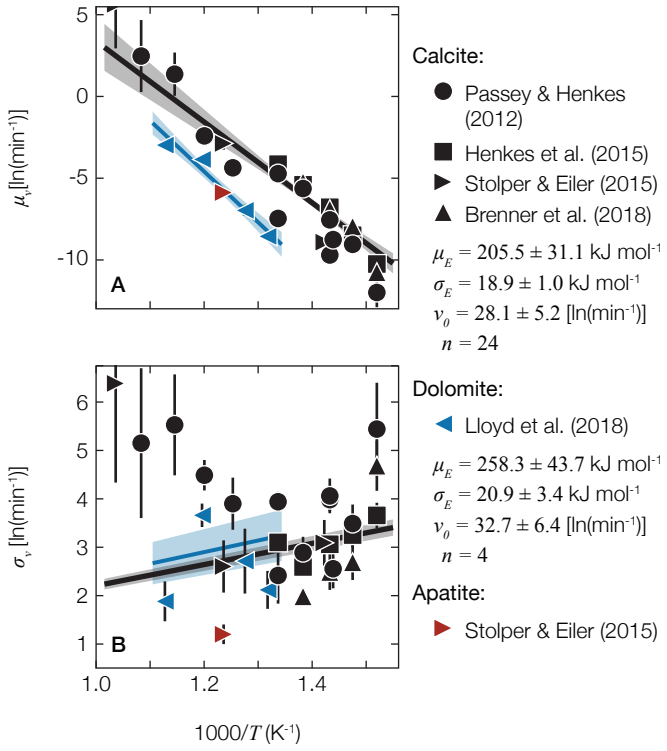

Figure S.3: Same as Fig. 5, but calculated using the T vs. $\Delta_{47}^{eq}(T)$ relationship from Lloyd et al. (2018) (their Eq. 4). (**A**) μ_ν and (**B**) σ_ν as a function of inverse experimental temperature. Arrhenius regression best-fit lines calculated using Eq. 27 for calcite (solid black line) and dolomite (solid blue line) are also shown, including $\pm 1\sigma$ uncertainty about each regression line (shaded regions). Experiments exhibiting noisy data [i.e., $\Delta_{47}(t)$ signal-to-noise < 5] or non-monotonic $\Delta_{47}(t)$ evolution were excluded from regressions and thus are not shown here (see Sec. 5.3 and Table S.3).

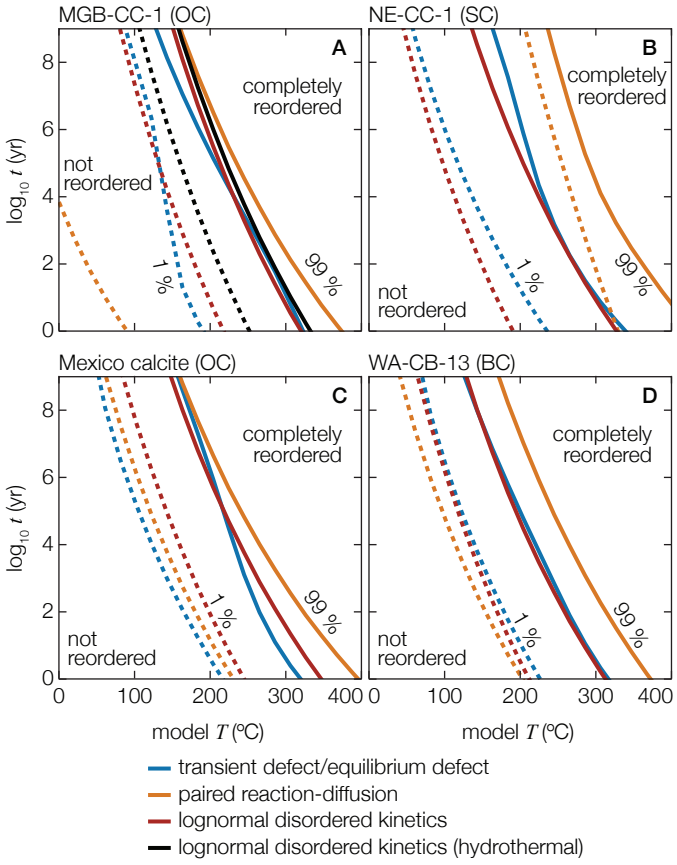

Figure S.4: Time-temperature fields for Δ_{47} preservation. Same as Fig. 8B, but calculated here for individual calcite minerals: (**A**) MGB-CC-1 optical calcite (data from Passey and Henkes, 2012), (**B**) NE-CC-1 spar calcite (data from Passey and Henkes, 2012), (**C**) Mexican optical calcite (data from Stolper and Eiler, 2015), (**D**) WA-CB-13 brachiopod shell calcite (data from Henkes et al., 2014). To generate each line, material that is initially described by $T(\Delta_{47})$ = 25 °C is assumed to be instantaneously heated and held at a given temperature; dotted lines indicate the time until incipient (1%) isotopologue reordering, which is conservative and may be below the detection limit given typical precision on natural samples, whereas solid lines indicate the time until complete (99%) isotopologue reordering at that temperature. Where available, predictions were generated using kinetic values for each model as reported in their original publications (Henkes et al., 2014; Stolper and Eiler, 2015). In some cases, model parameters for certain minerals have not been previously reported (transient defect/equilibrium defect: NE-CC-1, Mexican optical calcite; paired reaction-diffusion: NE-CC-1) and were calculated here by fitting the original heating experiment data using the 'isotopolog' python package (Hemingway, 2020). blue = transient defect/equilibrium defect (Henkes et al., 2014), orange = paired reaction-diffusion (Stolper and Eiler, 2015), black = lognormal disordered kinetics, hydrothermal conditions (this study; sample MGB-CC-1 only; data from Brenner et al., 2018), red = lognormal disordered kinetics (this study).